

The Thermodynamic Limit of Indoor Photovoltaics Based on Energetically-Disordered Molecular Semiconductors

Austin M. Kay¹, Maura E. Fitzsimons¹, Gregory Burwell¹, Paul Meredith¹, Ardalan Armin¹, and Oskar, J. Sandberg¹

¹Sustainable Advanced Materials (Sêr-SAM), Centre for Integrative Semiconductor Materials (CISM), Department of Physics, Swansea University Bay Campus, Swansea SA1 8EN, United Kingdom

Email: ardalan.armin@swansea.ac.uk; o.j.sandberg@swansea.ac.uk

Keywords: Indoor Photovoltaics, Internet-of-Things, Power Conversion Efficiency, Organic Photovoltaics, Radiative Losses, Non-Radiative Losses, Open-Circuit Voltage

Abstract

The coming decades are expected to host the advent of the ubiquitous “Internet-of-Things”, in which countless networked devices and sensors will perform all manner of tasks. Amongst the energy harvesting techniques that could provide locally-generated power to the Internet-of-Things, indoor photovoltaics (IPVs) show considerable promise. However, the bespoke emission spectra of artificial light sources present numerous challenges for designing and optimizing IPv, including determining the optimal bandgap, which is generally larger than the bandgaps of conventional semiconductors like silicon. In this regard, organic semiconductors are particularly desirable for IPv due to their tailorabile optical properties. We are, however, only just beginning to understand how to optimize organic semiconductor-based IPv at both material and device levels. Thus motivates this work, in which we explore how non-radiative open-circuit voltage losses, sub-optical gap absorption, and energetic disorder detrimentally affect the performance of organic semiconductor-based IPv. We present a realistic upper estimate for the power conversion efficiency (PCE) in the thermodynamic limit. We also describe a methodology (accompanied by a computational tool with a graphical user interface) for predicting IPv performance under arbitrary

illumination conditions. Using this methodology, we estimate the indoor PCEs of several photovoltaic materials, including the state-of-the-art systems PM6:Y6 and PM6:BTP-eC9.

1. Introduction

A recent coalescence of several technological trends has led to rapid developments in low-power networked devices. These trends include advancements in the fields of sensing, low-power electronics, communication protocols, machine learning, and more. Just as the World Wide Web irreversibly transformed communication in the late 20th century, the “Internet-of-Things” (IoT) is poised to revolutionize almost all sectors of the global economy.^[1,2] As early as 2025, it is expected that more data will originate from devices connected to the IoT than people.^[3] Extrapolating further into the future, the potential implications for societal challenges, such as healthcare, agriculture, the environment, and infrastructure, are immense.

The approaching ubiquity of IoT devices in our homes and workspaces necessitates the understanding of their environmental and social impacts.^[4, 5] Although individual devices may consume less than a microwatt of power, their aggregate energy consumption and environmental footprint should be carefully considered as these devices proliferate.^[6] Arguably, the most sustainable approach to powering IoT devices is to harness the ambient energy in their local environments using energy harvesting techniques. Such techniques, including piezoelectric, thermoelectric, and electromagnetic energy harvesting, have increasingly been topics of intensive investigation.^[7-10] This is not only because energy harvesting techniques mitigate the footprint of IoT devices associated with non-renewable sources of energy, but also because they reduce reliance on disposable batteries containing increasingly-rare materials. Consequently, self-powered devices can reduce the installation and maintenance costs associated with deploying IoT infrastructure.

At typical illumination levels of ambient light, indoor photovoltaics will generate sufficient power for emerging IoT devices in most settings.^[11] The development of indoor photovoltaics is propelled by progress in efficient charge controllers and supercapacitors, extending their viability for powering IoT

devices to situations where illumination is not continuous.^[12] Among other technological considerations, the lower light intensities and milder environments usually present indoors also provide less challenges for developing indoor photovoltaics with enhanced longevities.^[11, 13]

From a material optimization perspective, the criteria that indoor photovoltaics are benchmarked against differ in several ways from those used for conventional photovoltaics. These differences stem from the fact that the emission spectra and irradiances of artificial sources, such as light-emitting diodes (LEDs), are quite unlike the standard AM1.5G spectrum of sunlight. In general, the emission spectra of artificial light sources are centered at higher photon energies than the sunlight spectrum, they have narrower spectral peaks, and their irradiances are usually at least three orders of magnitude lower. Because of these differing spectral characteristics, the optimal semiconductor energy gap needed for indoor photovoltaic applications is generally larger than the bandgaps of conventional materials. For a given spectrum, this optimal gap is commonly estimated using the Shockley-Queisser (SQ) model, as it provides the maximum, thermodynamic limit of the power conversion efficiency (PCE) for a single-junction device with a sharp energy gap.

Under indoor conditions, the SQ model predicts PCEs surpassing 50% – significantly larger than the predicted PCE of 33.7% for AM1.5G sunlight.^[14, 15] To achieve such theoretically-high PCEs, indoor photovoltaics require optical gaps between 1.7 eV and 1.9 eV, considerably wider than the bandgaps of typical solar cell materials such as crystalline silicon (1.1 eV), gallium arsenide (1.42 eV), and cadmium telluride (1.44 eV).^[16] As such, alternative wide-gap semiconductors are urgently needed for use in indoor applications. Next-generation, molecular semiconductors exhibit several attributes that make them desirable for such applications, including mechanical and form factor flexibility, low embodied energy manufacturing, and the fact that they are amenable to solution-based fabrication techniques like spin-coating and roll-to-roll printing.^[17, 18] Of these, organic semiconductors are of particular technological-relevance for indoor applications because of the vast palette of materials available and the tunability afforded by synthetic organic chemistry.^[19-22]

In recent years, the performance of organic photovoltaics (OPVs) based on combinations of polymeric donors and low-offset, non-fullerene (small molecule) acceptors (NFAs) has advanced considerably.^[23-28] OPV materials and device architectures, however, are not yet optimized for applications, due in part to the relative infancy of the field and the lack of established measurement standards.^[29-31] The maximum, experimentally-determined PCE reported for an indoor photovoltaic device based upon conventional OPV principles is around 31%, whereas typical PCEs are on the order of 20% – considerably lower than the thermodynamic limit calculated via the SQ model.^[32, 33] Which therefore brings into question whether or not the PCEs of indoor photovoltaics predicted by the SQ model are realistically achievable, particularly for organic semiconductor-based systems. A thorough investigation of the thermodynamic limits of existing OPVs for indoor applications is therefore required for two reasons. Firstly, such an investigation would provide a roadmap for next-generation indoor photovoltaic development, including which routes for device optimization should be pursued. Secondly, it would provide a benchmark for indoor photovoltaic device characterization – before relevant standards are established, inter-laboratory comparisons are complicated by sources of uncertainty and error.^[29] These include variations in the spectra and irradiances used to simulate indoor illuminations – all too common problems encountered in the early days of organic solar cells designed for outdoor power generation, but re-emerging now for indoor photovoltaics.

To obtain realistic predictions for the maximum PCEs and optimal gaps of indoor photovoltaics based on organic semiconductors, the associated loss mechanisms of OPV devices need to be audited.^[12] This includes accounting for the excitonic nature of OPVs, as well as the associated static disorder that correlates with a broadened absorption onset and increased sub-gap absorption.^[34-36] In general, absorption well below the optical gap induces radiative losses in the open-circuit voltage. Sub-gap absorption is typically correlated with a so-called Urbach energy (E_U) – a measure of the exponential decay in absorption with decreasing photon energy (E).^[37, 38] As a result, OPVs with lower energetic disorder and smaller E_U are likely to have reduced open-circuit voltage losses and, consequently, higher PCEs.^[25, 39, 40] In addition

to the radiative open-circuit voltage losses induced by sub-gap absorption, further non-radiative open-circuit voltage losses are present in OPVs due to the intrinsic prevalence of non-radiative recombination.^[41-43] The electroluminescent external quantum efficiency (EQE_{EL}) is commonly used to estimate these non-radiative open-circuit voltage losses.^[44] While numerous processes can contribute to the non-radiative recombination in OPVs, the associated voltage loss has been found to generally correlate with the energy gap.^[41, 43]

In this work, we make realistic predictions for the PCEs of existing OPVs in indoor settings. We explore the effects of the optical gap and energetic disorder on the optimal PCE. In addition, we investigate the role of non-radiative open-circuit voltage losses, while accounting for the energy gap dependence of non-radiative recombination using an optimistic-yet-realistic empirical model guided by literature OPV data. Following this, we present a methodology and an accompanying computational tool (with an accessible graphical user interface) for estimating how a given photovoltaic system might perform under arbitrary illumination conditions. Utilizing this methodology, which employs measurements of a device's photovoltaic external quantum efficiency spectrum and its open-circuit voltage under AM1.5G conditions, we predict the indoor performance of emerging OPV systems. Finally, we demonstrate that the "fruit fly" systems PM6:Y6 and PM6:BTP-eC9 are likely limited to PCEs below 20% in indoor settings.

2. Results and Discussion

2.1. Photovoltaic Figures-of-Merit

The spectral fingerprints of artificial sources of light generally differ from source to source, displaying variations in intensity and separation of emission peaks. In **Figure 1a**, the spectral photon flux densities (Φ_{source}) of typical indoor light sources, including the 'warm white' 2700K LED and 'cool white' 4000K LED, are illustrated alongside the International Commission on Illumination's (CIE's) standard illuminant LED-B4. Therein, the integrated power density of each source, $P_{\text{source}} = \int_0^{\infty} E \Phi_{\text{source}}(E) dE$, is scaled to a total illuminance of 500 lux (see **Section S1 of the Supporting Information**). The corresponding scaled

AM1.5G spectrum has been included for comparison. In this work, we primarily consider the CIE LED-B4 standard as the indoor light source. However, it should be noted that the obtained findings are mostly independent of the used LED source, similar results are found for the 2700K LED and 4000K LED spectra (see **Supporting Information**).

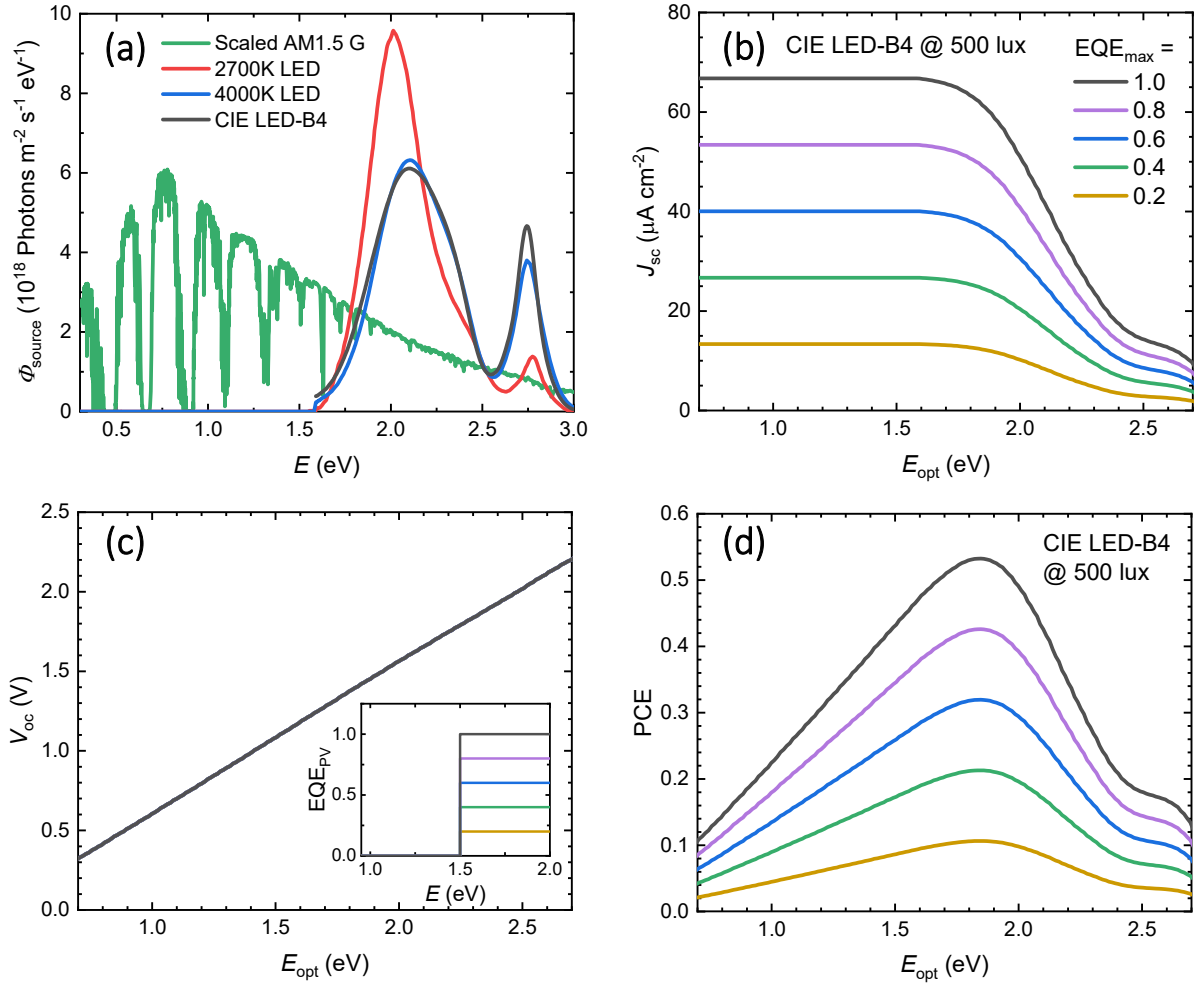


Figure 1: (a) The scaled AM1.5G spectrum for sunlight (green), the 2700K LED spectrum (red), the 4000K LED spectrum (blue), and the CIE LED-B4 spectrum (black), all plotted against the photon energy at an illuminance of 500 lux. In (b), (c), and (d), the short-circuit current density, the open-circuit voltage, and the power conversion efficiency under the LED-B4 spectrum at 500 lux, respectively, are plotted against

the optical gap for varied EQE_{\max} , assuming the step-function model for EQE_{PV} given by Equation (6).

The effect of increasing EQE_{\max} is illustrated for an optical gap $E_{\text{opt}} = 1.5$ eV in the inset graph in (c).

Under illumination, a photovoltaic device will generate power at efficiency^[16]

$$\text{PCE} = \frac{\text{FF} J_{\text{sc}} V_{\text{oc}}}{P_{\text{source}}}. \quad (1)$$

Here, V_{oc} is the open-circuit voltage, J_{sc} is the short-circuit current density, and FF is the fill factor. In general, the open-circuit voltage and the short-circuit current density relate to the device's photovoltaic external quantum efficiency $\text{EQE}_{\text{PV}}(E)$ (the ratio of the number of collected charge carriers to the number of incident photons at a given photon energy E) via^[16]

$$V_{\text{oc}} = \frac{kT}{q} \ln \left[1 + \frac{J_{\text{sc}}}{J_0} \right], \quad (2)$$

$$J_{\text{sc}} = q \int_0^{\infty} \text{EQE}_{\text{PV}}(E) \Phi_{\text{source}}(E) \, dE. \quad (3)$$

Wherein k denotes the Boltzmann constant, q the elementary charge, and T the temperature. The quantity J_0 , on the other hand, is the dark saturation current density. It is calculated using $J_0 = J_0^{\text{rad}} / \text{EQE}_{\text{EL}}$, where the radiative dark saturation current density (J_0^{rad}) is defined by^[44]

$$J_0^{\text{rad}} = q \int_0^{\infty} \text{EQE}_{\text{PV}}(E) \Phi_{\text{bb}}(E) \, dE, \quad (4)$$

where $\Phi_{\text{bb}}(E)$ is the spectral photon flux density of the ambient black-body radiation. Note that the device's EQE_{EL} equals one in the radiative limit, giving $J_0 = J_0^{\text{rad}}$ while $V_{\text{oc}} = V_{\text{oc}}^{\text{rad}}$ ($V_{\text{oc}}^{\text{rad}}$ is the corresponding radiative V_{oc}). Photovoltaic devices are generally far from the radiative limit; non-radiative recombination increases J_0 which, in turn, reduces the open-circuit voltage as $V_{\text{oc}} = V_{\text{oc}}^{\text{rad}} - \Delta V_{\text{oc}}^{\text{nr}}$, where $\Delta V_{\text{oc}}^{\text{nr}}$ is the associated non-radiative open-circuit voltage loss given by $\Delta V_{\text{oc}}^{\text{nr}} = -\frac{kT}{q} \ln(\text{EQE}_{\text{EL}})$ for $V_{\text{oc}} \gg kT/q$.^[44]

In our analysis we have assumed that the current density can be well-approximated by the ideal Shockley-diode equation.^[16] Under these conditions, the fill factor FF can be determined using a Lambert

W function approach. This approach is herein employed (see **Section S2 of the Supporting Information**), and in the computational tool we provide as **Supporting Material** as well. However, we note that for V_{oc} larger than 0.5 V, the fill factor is well-approximated by^[45]

$$FF \approx \frac{\frac{qV_{oc}}{kT} - \ln\left(1 + \frac{qV_{oc}}{kT}\right)}{1 + \frac{qV_{oc}}{kT}}. \quad (5)$$

This suggests that the leading-order behavior of the fill factor is primarily determined by the open-circuit voltage. Consequently, minimizing open-circuit voltage losses is of paramount importance for realizing high-PCE indoor photovoltaics based on organic semiconductors.

2.2. Effect of Radiative Open-Circuit Voltage Losses

We now consider the influence of radiative open-circuit voltage losses on the performance of indoor photovoltaics by firstly discussing the idealized case of a sharp optical gap and no sub-gap absorption. In this case, EQE_{PV} can be modelled using a step function, where all photons of energy greater than or equal to a threshold optical gap (E_{opt}) generate a collected electron-hole pair at efficiency EQE_{max} , whereas photons of energy less than the optical gap do not:

$$EQE_{PV}(E) = \begin{cases} EQE_{max}, & \text{if } E \geq E_{opt}, \\ 0, & \text{otherwise.} \end{cases} \quad (6)$$

The photovoltaic external quantum efficiency in the SQ model is defined using this equation in the ideal case that $EQE_{max} = 1$.^[15] For an EQE_{PV} modeled using Equation (6), the short-circuit current density, radiative open-circuit voltage, and resultant PCE under the CIE LED-B4 spectrum at 500 lux are shown for varying EQE_{max} in **Figure 1b, c, and d**, respectively. As shown, at a particular optical gap, the short-circuit current density is directly proportional to EQE_{max} . The open-circuit voltage, however, is independent of EQE_{max} and so the V_{oc} curves are perfectly aligned and equal to the open-circuit voltage predicted by the SQ model (V_{oc}^{SQ}). Since the FF is predominantly determined by the V_{oc} , the PCE scales in a similar way to J_{sc} , changing linearly with EQE_{max} .

From **Figure 1d**, it is evident that in the SQ model, the maximum PCE under the CIE LED-B4 spectrum at 500 lux is 53%, obtained at an optical gap $E_{\text{opt}} = 1.83$ eV, with $V_{\text{oc}}^{\text{SQ}} = 1.41$ V and $J_{\text{sc}} = 62.1 \mu\text{A cm}^{-2}$. However, for current state-of-the-art OPVs, the empirical upper limit of the EQE_{PV} is closer to 0.85. Therefore, to realistically estimate the PCEs of indoor photovoltaics based on organic semiconductors, an above-gap photovoltaic quantum efficiency of $\text{EQE}_{\text{max}} = 0.85$ is herein assumed – unless explicitly stated otherwise – as this value describes realistically-high performance. The corresponding maximum PCE for $\text{EQE}_{\text{max}} = 0.85$ is reduced to 45.3%, which is still obtained at $E_{\text{opt}} = 1.83$ eV (for CIE LED-B4 at 500 lux).

Despite being rudimentary, the step-function model given by Equation (6) is a good approximation for EQE_{PV} in semiconductors with well-defined band edges, such as crystalline, inorganic semiconductors. Many photovoltaic materials, however, are not well-described by the highly-idealized step-function model. A more realistic prediction for the PCEs of indoor photovoltaics based on energetically-disordered materials, including OPVs, must account for the inherent, static energetic disorder associated with the density of states. As increased static energetic disorder broadens the effective band edges and leads to increased sub-gap absorption, it will increase radiative open-circuit voltage losses and reduce the PCE.

Sub-gap absorption in disordered materials is commonly described by a tail that decays exponentially with decreasing photon energy below the gap. This tail may be designated a characteristic energy – the aforementioned Urbach energy (E_{U}).^[38] Consequently, a more realistic model for EQE_{PV} in many photovoltaics is given by

$$\text{EQE}_{\text{PV}}(E) = \text{EQE}_{\text{max}} \begin{cases} 1, & \text{if } E \geq E_{\text{opt}}, \\ \exp\left(\frac{E - E_{\text{opt}}}{E_{\text{U}}}\right), & \text{otherwise.} \end{cases} \quad (7)$$

The Urbach energy correlates with the level of disorder in a system and, as illustrated in **Figure 2a**, it determines the gradient of the exponential decay of the sub-gap tail. A reasonable minimum value for the

Urbach energy of OPVs is the thermal energy (kT); throughout the remainder of this work we assume $kT = 25.3$ meV (corresponding to $T = 20^\circ\text{C} = 293.15$ K).^[34]

The presence of sub-gap Urbach tails gives rise to a decrease in $V_{\text{oc}}^{\text{rad}}$, as shown in **Figure 2b**. In **Figure 2c**, it is shown that these losses, in turn, reduce the maximum power conversion efficiency from 45% to just 20% (in the $E_{\text{U}} = 50$ meV case), while concurrently blue-shifting the best-performing E_{opt} from 1.83 eV to 1.90 eV. Material systems with high E_{U} therefore require larger optical gaps to achieve high performance. We note that the short-circuit current density is found to be largely independent of E_{U} . The loss in PCE shown in Figure 2c is therefore a result of the radiative open-circuit voltage loss ($\Delta V_{\text{oc,sub-g}}^{\text{rad}}$) induced by sup-gap tails. This voltage loss is quantified by the deviation between $V_{\text{oc}}^{\text{SQ}}$ (determined in the SQ model) and the $V_{\text{oc}}^{\text{rad}}$ obtained in case of a sub-gap tail, $\Delta V_{\text{oc,sub-g}}^{\text{rad}} = V_{\text{oc}}^{\text{SQ}} - V_{\text{oc}}^{\text{rad}}$. For the open-circuit voltage curves of Figure 2b, these deviations were determined then plotted in **Figure 2d**. For $E_{\text{U}} \geq kT$, the optical gap-dependent behavior of these curves can be described by the following analytical approximations (see **Supporting Information**):

$$q\Delta V_{\text{oc,sub-gap}}^{\text{rad}} \approx \begin{cases} \left(1 - \frac{kT}{E_{\text{U}}}\right)E_{\text{opt}} + kT \ln \left[\frac{2(kT)^2}{E_{\text{opt}}^2 \left(1 - \frac{kT}{E_{\text{U}}}\right)^3} \right], & \text{if } E_{\text{U}} > kT. \\ kT \ln \left[\frac{E_{\text{opt}}}{3kT} + 1 \right], & \text{if } E_{\text{U}} = kT. \end{cases} \quad (8)$$

Equation (8) describes $\Delta V_{\text{oc,sub-gap}}^{\text{rad}}$ well for $E_{\text{U}} \geq kT$ at typical optical gaps, as shown by the dashed curves in Figure 2d.

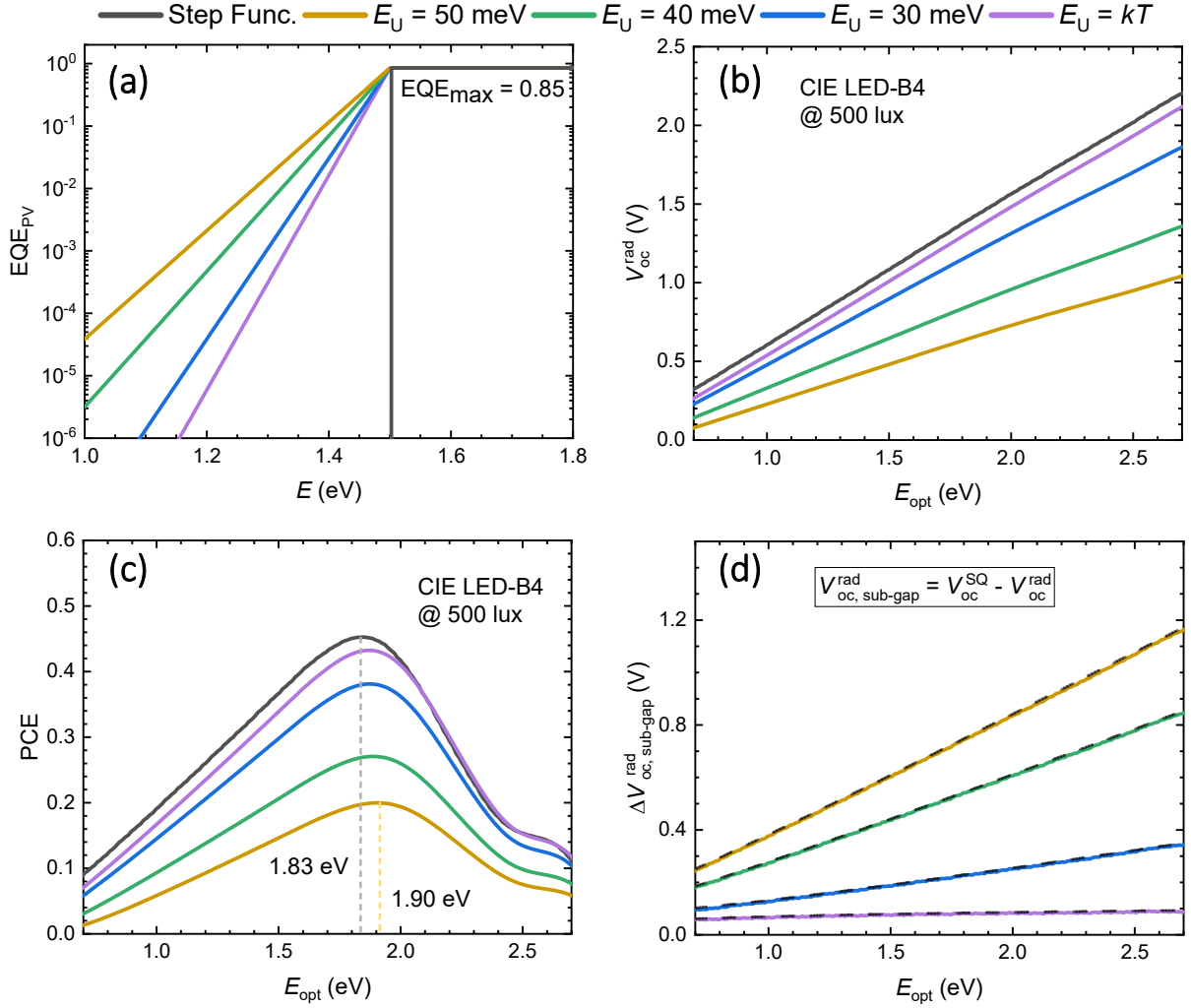


Figure 2: Investigating the effect of sub-gap tails of varying Urbach energy on the open-circuit voltage and the power conversion efficiency. **(a)** Photovoltaic external quantum efficiency spectra centered at an optical gap $E_{\text{opt}} = 1.5 \text{ eV}$, with $\text{EQE}_{\text{max}} = 0.85$ and E_U varied from 0 (step function) to 50 meV. **(b)** The resultant open-circuit voltages in the radiative limit, plotted as a function of the optical gap. **(c)** The PCE under the CIE LED-B4 spectrum at 500 lux, plotted as a function of the optical gap for a variety of Urbach energies. **(d)** The solid curves indicate the numerically-calculated deviations between the open-circuit voltage in the SQ model and the sub-gap Urbach tail model. The dashed lines indicate the corresponding analytical approximation given by Equation (8).

Previously, the static energetic disorder in organic semiconductors has also been frequently modelled in terms of a Gaussian distribution of states. Consistent with this, the EQE_{PV} associated with excitonic sub-gap absorption in several low-offset NFA OPV material systems was recently found to be well-described by^[34, 36]

$$\text{EQE}_{\text{PV}}(E) = \frac{\text{EQE}_{\text{max}}}{2} \left\{ \exp \left[\frac{E - E_{\text{opt}} + \frac{\sigma_s^2}{2kT}}{kT} \right] \text{erfc} \left[\frac{E - E_{\text{opt}} + \frac{\sigma_s^2}{kT}}{\sigma_s \sqrt{2}} \right] + \text{erfc} \left[\frac{E_{\text{opt}} - E}{\sigma_s \sqrt{2}} \right] \right\}, \quad (9)$$

where E_{opt} is the centre of a Gaussian distribution of exciton states with static disorder parameter σ_s . Here, $\text{erfc}(x)$ denotes the complementary error function. The spectral behavior of Equation (9) at different σ_s is illustrated in **Figure 3a** for $\text{EQE}_{\text{max}} = 0.85$ and an optical gap of 1.5 eV. For energies well below the gap ($E \ll E_{\text{opt}}$), Equation (9) reduces to a sub-gap Urbach tail with $E_U = kT$. Above the gap, on the other hand, a saturation is reached wherein $\text{EQE}_{\text{PV}}(E) \rightarrow \text{EQE}_{\text{max}}$. Between these two regimes lies a transition regime with a shape and spectral broadness determined by σ_s .

Figure 3b and **3c** show the $V_{\text{oc}}^{\text{rad}}$ and PCE as a function optical gap obtained based on the EQE_{PV} (Equation (9)) from Figure 3a. The corresponding radiative open-circuit voltage losses $\Delta V_{\text{oc,sub-gap}}^{\text{rad}}$, induced by the sub-gap EQE_{PV} , are shown in **Figure 3d**. As illustrated throughout **Figure 3**, a higher static energetic disorder gives rise to increased radiative open-circuit voltage loss, thereby reducing the power conversion efficiency from 45% in the step function model to 36% in the $\sigma_s = 100$ meV case. In addition, the best-performing optical gap is once again blue-shifted from 1.83 eV to 1.88 eV in this case.

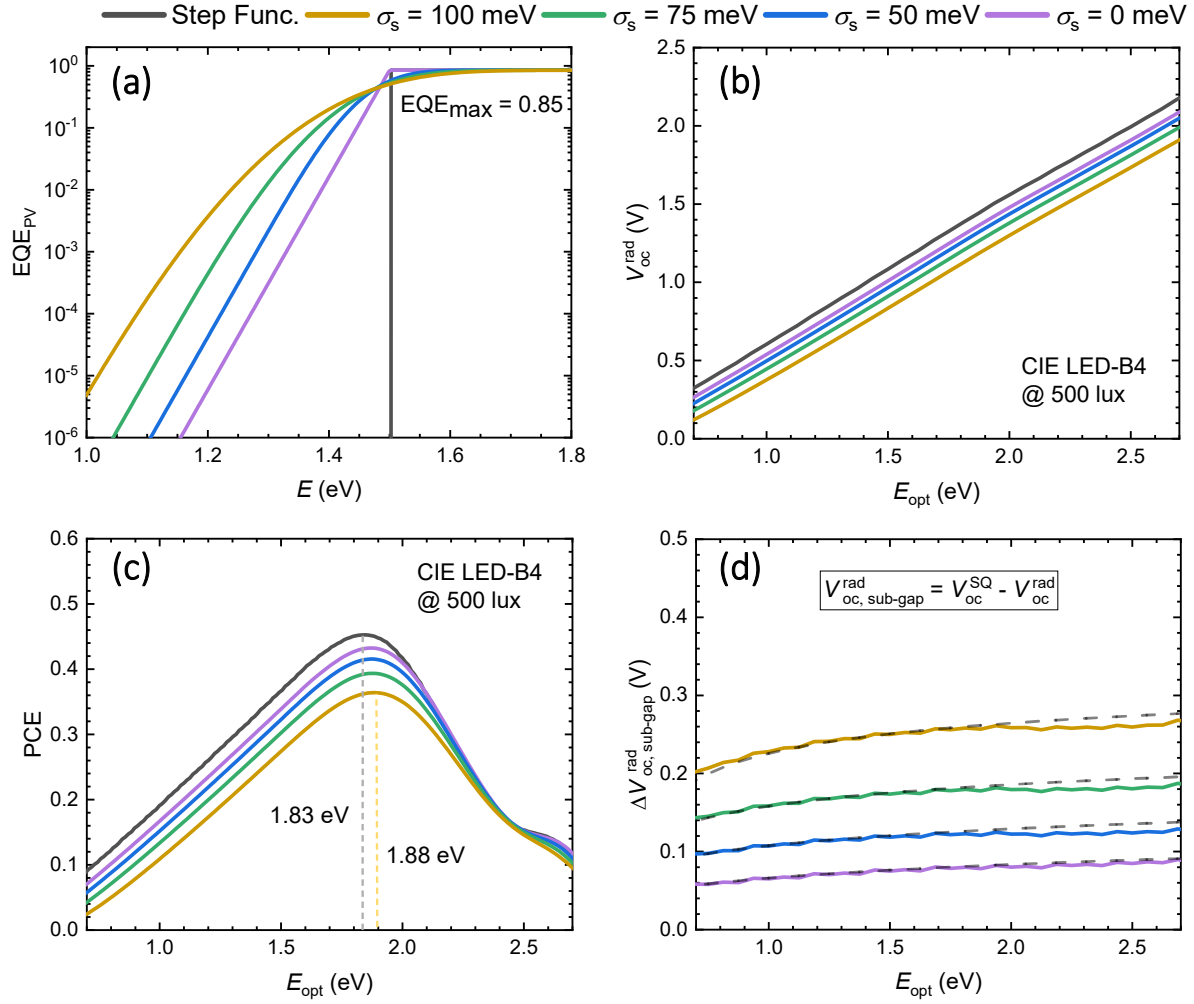


Figure 3: Investigating the effect of energetic disorder on the open-circuit voltage and the power conversion efficiency. **(a)** Photovoltaic external quantum efficiency spectra centered at an optical gap $E_{\text{opt}} = 1.5 \text{ eV}$, with $\text{EQE}_{\text{max}} = 0.85$ and σ_s varied from 0 meV to 100 meV, plotted alongside the step function model for EQE_{PV} (in black). **(b)** The resultant open-circuit voltages in the radiative limit, plotted as a function of the optical gap. **(c)** The PCE under the CIE LED-B4 spectrum at 500 lux, plotted as a function of the optical gap for varying σ_s . **(d)** The solid curves indicate the numerically-calculated deviations between the open-circuit voltage in the SQ model and the OPV model, where EQE_{PV} is modelled in the latter using Equation (9). The dashed lines indicate the analytical approximation given by Equation (10).

As with the varied Urbach energy case, an analytical approximation for $\Delta V_{\text{oc,sub-gap}}^{\text{rad}}$ for the case of a sub-gap EQE_{PV} given by Equation (9) can be obtained assuming that the short-circuit current density is invariant of σ_s and solely determined by the contribution from the above-gap EQE_{PV} (see **Section S5** of the **Supporting Information**). Under such conditions, $\Delta V_{\text{oc,sub-g}}^{\text{rad}}$ can be obtained from

$$q\Delta V_{\text{oc,sub-gap}}^{\text{rad}} \approx \frac{\sigma_s^2}{2kT} + kT \ln \left[\frac{E_{\text{opt}}}{3kT} \left(1 - \frac{\sigma_s^2}{E_{\text{opt}}kT} \right)^3 \right]. \quad (10)$$

This analytical approximation is indicated by the dashed lines in **Figure 3d**. As shown, the approximation agrees well with the numerically-calculated results for typical optical gaps.

2.3. Effect of Non-Radiative Open-Circuit Voltage Losses

In real photovoltaic devices, the open-circuit voltage is further reduced by non-radiative recombination, which reduces EQE_{EL} below unity and gives rise to a non-zero non-radiative open-circuit voltage loss $\Delta V_{\text{oc}}^{\text{nr}}$.^[41, 44, 46] In OPVs, the non-radiative open-circuit voltage loss measured under one Sun has been observed to increase with decreasing energy gap, consistent with the energy-gap law.^[41, 43, 44, 46] This is demonstrated in **Figure 4a**, where experimental $\Delta V_{\text{oc}}^{\text{nr}}$ data compiled by Ullbrich et al.^[41] is plotted against the energy of the CT state (E_{CT}), which we take as a proxy for E_{opt} (valid for low-offset, NFA OPV blends). Additional data points for systems with fullerene acceptors and NFAs are plotted as blue squares and green triangles, respectively. We note that at light intensities representative of indoor settings, the non-radiative loss may, in general, be larger (due to additional trap-assisted recombination); as such, the data in **Figure 4a** could be considered as a realistic upper estimate of $\Delta V_{\text{oc}}^{\text{nr}}$ in organic semiconductor-based indoor photovoltaics.

To obtain a realistic estimate of non-radiative open-circuit voltage losses in state-of-the-art OPVs, we have designed an empirical, qualitative model for $\Delta V_{\text{oc}}^{\text{nr}}$ based on the experimental data in **Figure 4a**. In this empirical model, $\Delta V_{\text{oc}}^{\text{nr}}$ is modelled as a quadratic of the form

$$\Delta V_{\text{oc}}^{\text{nr}} = \begin{cases} AE_{\text{opt}}^2 + BE_{\text{opt}} + C, & \text{if } E_{\text{opt}} \leq 2.601 \text{ eV}, \\ 0.0945 \text{ V}, & \text{otherwise,} \end{cases} \quad (11)$$

where the optical gap has units of eV, and the coefficients are $A = 0.123 \text{ V}/(\text{eV})^2$, $B = -0.64 \text{ V}/(\text{eV})$, and $C = 0.927 \text{ V}$. The transition at 2.601 eV prevents $\Delta V_{\text{oc}}^{\text{nr}}$ from growing again after the parabola reaches its minimum. We stress that this optimistic-yet-realistic model (illustrated by the red curve in **Figure 4a**) has no underlying theoretical framework – it is just a means for encapsulating the general trend shown by the experimental data in Figure 4a. For comparison, another semi-analytical model for $\Delta V_{\text{oc}}^{\text{nr}}$ based on the work of Benduhn et al. is included in Figure 4a.^[46] In this model, where a negligibly-small reorganization energy has been assumed, $\Delta V_{\text{oc}}^{\text{nr}}$ relates to E_{CT} via the so-called energy gap law:

$$\Delta V_{\text{oc}}^{\text{nr}} \approx C - DE_{\text{CT}} \approx C - DE_{\text{opt}}, \quad (12)$$

where, $C = 0.574 \text{ V}$ and $D = 0.184 \text{ V eV}^{-1}$.

The effect of the two non-radiative open-circuit voltage loss models on the open-circuit voltage and PCE are illustrated in **Figure 4b** and **Figure 4c**, respectively. To simulate these curves, a step-function EQE_{PV} was used with EQE_{max} = 0.85. It is evident from these curves that accounting for realistic non-radiative open-circuit voltage losses reduces the maximum PCE from 45% to around 40%, while blue-shifting the highest-performing optical gap from 1.83 eV to 1.88 eV. Comparable results are produced by both the semi-analytical energy gap law model given by Equation (12) and the optimistic, empirical model given by Equation (11). However, as the PCE differs by just a few percent between the models, we herein utilize Equation (11) to model non-radiative losses to make the most optimistic prediction for indoor photovoltaic performance.

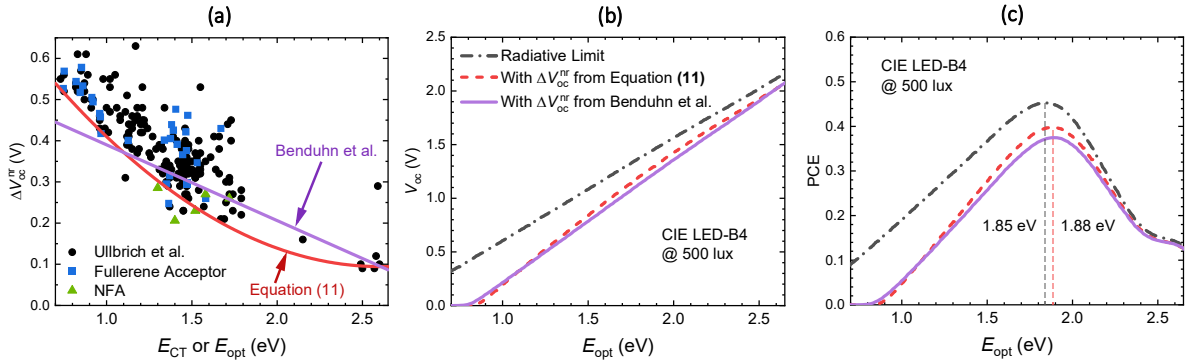


Figure 4: The effect of non-radiative open-circuit voltage losses on the PCE of indoor photovoltaics. **(a)** Non-radiative open-circuit losses as a function of the energy of the CT state, E_{CT} , with experimental data compiled by Ullbrich et al. plotted as black squares.^[41] Additional data points for OPV blends with fullerene acceptors and NFAs are plotted as blue squares and green triangles, respectively. The empirical model for V_{oc}^{nr} given by Equation (11) is indicated by the solid curve. **(b)** The open-circuit voltage against the optical gap in the radiative limit (black dash-dot curve) and in two non-radiative open-circuit voltage loss models (red dashed curve for Equation (11) and solid purple curve for Equation (12)) calculated using the step function model for EQE_{OPV} with EQE_{max} = 0.85. **(c)** The resultant power conversion efficiencies under the CIE LED-B4 spectrum at 500 lux.

The predicted PCEs of organic semiconductor-based indoor photovoltaics, accounting for both radiative losses and non-radiative losses, are shown in **Figure 5** for the CIE LED-B4 spectrum. The OPV predictions (for both $\sigma_s = 0$ and $\sigma_s = 50$ meV) assume sub-gap absorption calculated using Equation (9) and additional ΔV_{oc}^{nr} loss given by Equation (11). Note that EQE_{max} = 0.85 was used to predict an optimistic upper limit for OPVs. The ideal radiative PCE limits based on the step-function model (Equation (6)) with EQE_{max} = 1 (i.e., the SQ model) and the more realistic EQE_{max} = 0.85 have been included for comparison. These four curves are plotted against the optical gap at an illuminance of 500 lux in **Figure 5a**, whereas, in **Figure 5b**, they are plotted against the illuminance of the incident light for the best-performing optical gap (which has been inset into the graph for each curve).

By accounting for sub-gap absorption, energetic disorder, and realistic non-radiative open-circuit voltage losses, we find that the maximum PCE of OPVs under CIE LED-B4 at 500 lux is reduced from its SQ model value of 53% to around 37%. Furthermore, the highest-performing E_{opt} is blue-shifted by around 80 meV. Corresponding discussions for the 2700K LED and 4000K LED sources are provided in **Section S6 of the Supporting Information.**

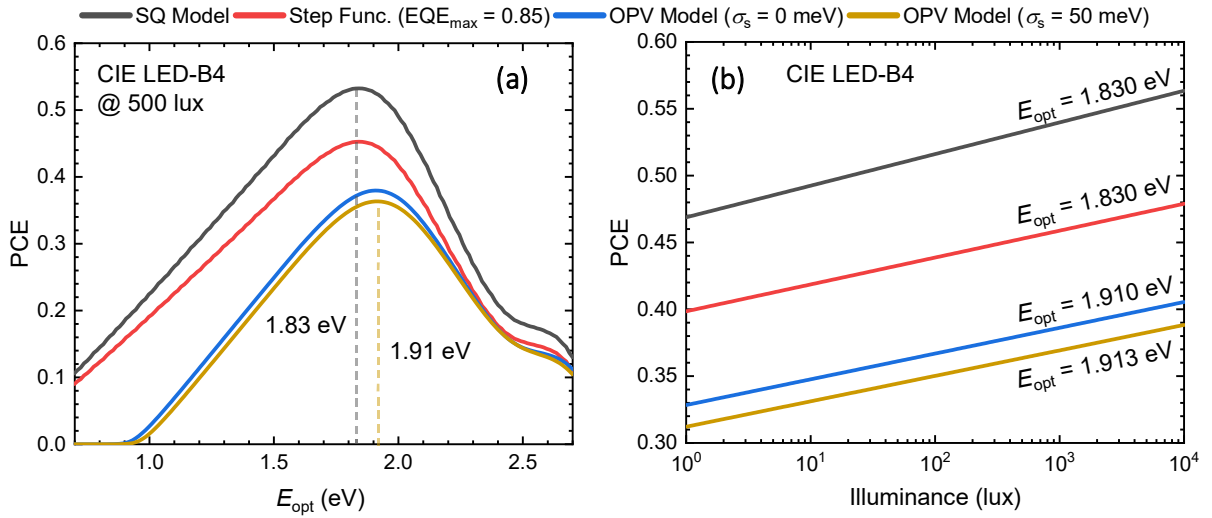


Figure 5: Power conversion efficiencies simulated under the CIE LED-B4 spectrum as a function of the optical gap in **(a)**, and as a function of the illuminance in **(b)**. In both panels, four curves are present. The black curve illustrates the PCE in the radiative SQ Model, while the red curve indicates the PCE when EQE_{PV} is modelled as a step function with $\text{EQE}_{\text{max}} = 0.85$. The blue and yellow curves, on the other hand, illustrate the realistic OPV model for $\sigma_s = 0$ and $\sigma_s = 50$ meV, respectively. In this model, EQE_{PV} is calculated using Equation (9) with $\text{EQE}_{\text{max}} = 0.85$ and $\Delta V_{\text{oc}}^{\text{nr}}$ is assigned for a given optical gap using Equation (11). In **(b)**, the highest-performing optical gaps used to simulate the curves are inset.

Based on Figure 5, an OPV blend with the highest-performing optical gap of $E_{\text{opt}} = 1.91$ eV and minimal energetic disorder will likely have a PCE lower than 40% at typical indoor light intensities (up to 5000 lux). Accounting for energetic disorder (typically on the order of $\sigma_s = 50$ meV) further reduces the PCE. To estimate the figures-of-merit of particular OPV materials in indoor settings more accurately, we

have devised a methodology and created an associated computational tool (with a graphical user interface) that takes an experimentally-determined EQE_{PV} spectrum and measured open-circuit voltage under one Sun (V_{oc}^{\odot}) as inputs. Using these components, the non-radiative open-circuit voltage loss can be calculated through

$$\Delta V_{oc}^{nr} \approx \frac{k_B T}{q} \ln \left(1 + \frac{J_{sc}^{\odot}}{J_0^{\text{rad}}} \right) - V_{oc}^{\odot}, \quad (13)$$

where J_{sc}^{\odot} is the short-circuit current density under one Sun (determined from EQE_{PV}). Assuming Equation (13) provides a realistic lower limit estimate of the device's ΔV_{oc}^{nr} , optimistic values for the photovoltaic figures-of-merit can then be estimated under any spectrum at any intensity. A block diagram detailing this methodology, including the identification of the true radiative open-circuit voltage in the thermodynamic limit, is shown in **Figure S8** of the **Supporting Information**.^[47]

2.4. Comparative Analysis

In **Figure 6a**, the PCE limits for the $\sigma_s = 0$ (OPV model), with EQE_{PV} based on Equation (9) and ΔV_{oc}^{nr} given by Equation (11), is compared to expected PCEs of state-of-the-art OPVs under CIE LED-B4. The idealized PCE (in the radiative limit) predicted by the SQ model and the step function EQE_{PV} with EQE_{max} = 0.85 have been included for comparison. The predicted PCEs of state-of-the-art OPV blends, [11, 34, 47-50] crystalline and amorphous silicon, and a single cation perovskite^[49] were estimated using measured EQE_{PV} spectra and V_{oc}^{\odot} from the literature. The corresponding optical gaps of the OPVs were determined using Equation (9) in the technique summarized in **Section S8** of the **Supporting Information**.^[36] To provide as realistic an estimate as possible for each photovoltaic material, the PCE has been scaled such that the short-circuit current density under one Sun matches the pre-eminent literature value; discussions on the determination of these values and how they were scaled with literature J_{sc} values are provided in **Section S9** and **Section S10** of the **Supporting Information**, respectively.

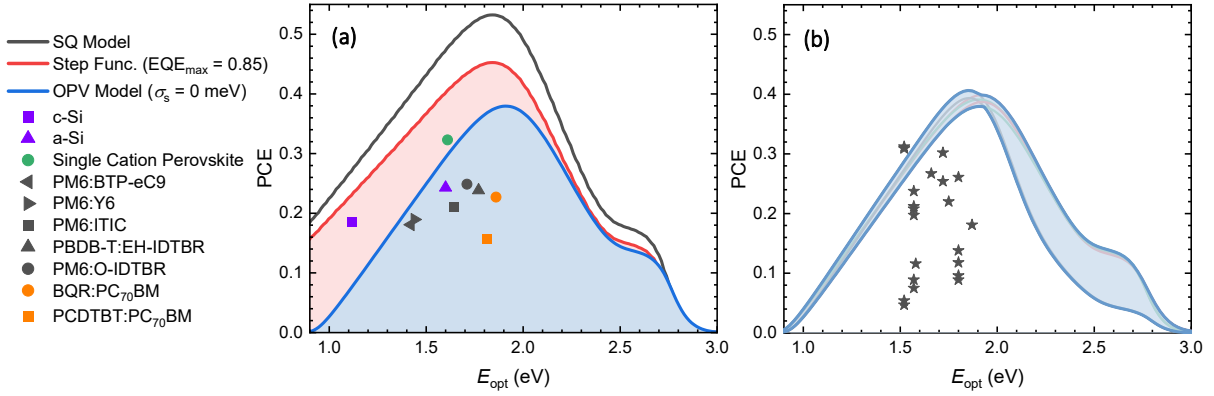


Figure 6: Power conversion efficiencies of current state of the art OPV material systems alongside more conventional inorganic semiconductors illuminated with indoor lighting conditions. **(a)** A comparison of estimated indoor behavior silicon photovoltaics (purple data points), a single cation perovskite (green data points), NFA OPV blends (black data points), and fullerene acceptor OPV blends (orange data points), with the PCE in the SQ model (black curve), the step function with $\text{EQE}_{\text{max}} = 0.85$ model (red curve), and the $\sigma_s = 0$ limit of the OPV model (blue curve). The red shaded region indicates a regime of optimal performance for materials with low energetic disorder and low $\Delta V_{\text{oc}}^{\text{nr}}$, whereas the blue shaded region indicates a realistic OPV regime. **(b)** PCE values from the literature, compared with the realistic OPV model as a function of the optical gap for the CIE LED-B4, 2700K LED, and 4000K LED sources, in the hypothetical $\sigma_s = 0$ case.

From the estimated PCEs of Figure 6a, it is evident that the state-of-the-art organic solar cell blends PM6:Y6 and PM6:BTP-eC9 (with $E_{\text{opt}} \sim 1.4$ eV) will likely not exceed PCEs of 20% in indoor settings unless the non-radiative losses can be drastically reduced. As previously discussed in Figure 5, this becomes more evident when accounting for energetic disorder (around 43 meV for both blends) as it further reduces the radiative limit. On the other hand, other OPV systems such as PBDB-T:EH-IDTBR and PM6:O-IDTBR, have a fair amount of room for improvement. This is particularly clear when comparing with experimentally-determined PCE values from the literature, as evidenced in **Figure 6b**. Alongside these data points, the PCE predicted by the realistic OPV model (with $\sigma_s = 0$) has been plotted for the CIE LED-B4,

2700K LED, and 4000K LED spectra at both 500 lux and 2000 lux. An envelope has then been plotted to encapsulate the maximum PCE held by any of the spectra, providing a realistic estimate for PCE of indoor photovoltaics under *any* artificial spectrum. Based on this envelope, we can see that many of the OPV blends have room for improvement. We also note, however, that at least one data point from the literature defies the realistic OPV limit, despite the fact that the simulations were conducted at a higher illuminance. While it is plausible that this OPV system has very little non-radiative recombination, especially as Equation (11) predicts a larger ΔV_{oc}^{nr} than some of the literature data in Figure 4a, it is more likely that there were inaccuracies in the experimental set-up; this demonstrates not only the challenging task of measuring indoor PCEs, but also the urgent need for a tried and tested standard for indoor photovoltaics, including an accepted experimental methodology for characterizing the devices.

3. Conclusion

Indoor photovoltaics are rapidly proving to be a very practical application for organic semiconductors; they continue to be a promising contender for powering for the IoT using energy-harvesting techniques. There are, however, some inconsistencies in the literature regarding the PCEs of indoor photovoltaics, with some devices seemingly surpassing a generous limit; this is likely due to a lack of accepted testing standard for indoor photovoltaics. By presenting a realistic limit for the PCE of OPVs, which accounts for both radiative open-circuit voltage losses induced by sub-gap absorption (including Urbach tails and energetic disorder) and non-radiative open-circuit voltage losses, we aim to elucidate what PCEs could reasonably be expected. In particular, we have shown that a combination of realistic above-gap EQE_{PV} and ΔV_{oc}^{nr} , in combination with a typical energetic disorder ($\sigma_s = 50$ meV), can reduce the maximum PCE of OPVs from a SQ model value of 53% to 37% under indoor lighting conditions. We have also shown that the best-performing optical gap becomes blue-shifted from $E_{opt} = 1.83$ eV to 1.91 eV in the $\sigma_s = 50$ meV limit of the OPV model, suggesting that the high-performance OPV blends PM6:Y6 and PM6:BTP-eC9 may not exceed PCEs of 20% in indoor settings. To aid future work on indoor applications of OPVs, we have presented a methodology for estimating the performance of indoor photovoltaics at typical illuminances, using

measurements of the photovoltaic external quantum efficiency spectrum and the open-circuit voltage under one Sun. Furthermore, to automate the estimation of indoor photovoltaic performance under arbitrary illumination conditions using these quantities, we have provided a computational tool (with a graphical user interface) as **Supporting Material**.

4. The Computational Tool

To aid the estimation of the PCEs of particular photovoltaic materials, a computational tool was prepared in the open-source Python interactive development environment, Jupyter. While this is not the first computational tool for simulating photovoltaic figures-of-merit under indoor illumination conditions, it does have a few unique characteristics. Chief among these, this tool includes a detailed graphical user interface that can be used to control the simulations. To estimate indoor photovoltaic device performance, the tool allows the use of both simulated and experimentally-determined EQE_{PV} spectra; it can simulate step-functions, sub-gap Urbach tails, and OPV absorption using Equation (9). Using these EQE_{PV} spectra, the tool determines the photovoltaic figures-of-merit under a selected spectrum (e.g., CIE LED-B4) at any desired illuminance. A variety of non-radiative open-circuit voltage loss models are available, including Equation (11). The photon flux spectra used by the tool can be customized (and superimposed), and as many EQE_{PV} spectra as desired can be loaded in. Alongside the well-detailed tool, a manual has also been prepared that describes how to install Jupyter and how to navigate the user interface.

Acknowledgements

We kindly acknowledge Dr. Nasim Zarrabi, Dr. Stefan Zeiske, Dr. Christina Kaiser, and Dr. Wei Li, for providing experimental photovoltaic external quantum efficiency data. This work was funded through the Welsh Government’s Sêr Cymru II Program ‘Sustainable Advanced Materials’ (Welsh European Funding Office – European Regional Development Fund). P.M. is a Sêr Cymru II Research Chair and A.A. is a Rising Star Fellow also funded through the Welsh Government’s Sêr Cymru II ‘Sustainable Advanced Materials’ Program (European Regional Development Fund, Welsh European Funding Office and Swansea

University Strategic Initiative). This work was also funded by the UKRI through the EPSRC Program Grant EP/T028513/1 Application Targeted and Integrated Photovoltaics.

Data Availability Statement

The data that support the results of this work are available as **Supporting Material**.

Conflicts of Interest

The authors declare no conflicts of interest.

References

1. Atzori, L., A. Iera, and G. Morabito, *The Internet of Things: A Survey*. Computer Networks, **2010**. 54(15): p. 2787-2805.
2. Vermesan, O., P. Friess, P. Guillemin, R. Giaffreda, H. Grindvoll, M. Eisenhauer, M. Serrano, K. Moessner, M. Spirito, and L.-C. Blystad, *Internet of Things Beyond the Hype: Research, Innovation and Deployment*, in *Building the Hyperconnected Society-Internet of Things Research and Innovation Value Chains, Ecosystems and Markets*. **2022**, River Publishers. p. 15-118.
3. Intel. *Intelligent Decisions with Intel Internet of Things (IoT)*. Accessed: 18th January 2023]; Available from: <https://www.intel.co.uk/content/www/uk/en/internet-of-things/overview.html>.
4. Arshad, R., S. Zahoor, M.A. Shah, A. Wahid, and H. Yu, *Green IoT: An Investigation on Energy Saving Practices for 2020 and Beyond*. IEEE Access, **2017**. 5: p. 15667-15681.
5. Alsamhi, S.H., O. Ma, M. Ansari, and Q. Meng, *Greening Internet of Things for Greener and Smarter Cities: A Survey and Future Prospects*. Telecommunication Systems, **2019**. 72(4): p. 609-632.
6. I.E.A., *More Data, Less Energy*. **2014**.
7. Erturk, A. and D.J. Inman, *Piezoelectric Energy Harvesting*. **2011**: John Wiley & Sons.
8. Scholdt, M., H. Do, J. Lang, A. Gall, A. Colsmann, U. Lemmer, J.D. Koenig, M. Winkler, and H. Boettner, *Organic Semiconductors for Thermoelectric Applications*. Journal of Electronic Materials, **2010**. 39(9): p. 1589-1592.
9. Priya, S. and D.J. Inman, *Energy Harvesting Technologies*. Vol. 21. **2009**: Springer.
10. Pecunia, V., L.G. Occhipinti, and R.L.Z. Hoye, *Emerging Indoor Photovoltaic Technologies for Sustainable Internet of Things*. Advanced Energy Materials, **2021**. 11(29): p. 2100698.
11. Burwell, G., O.J. Sandberg, W. Li, P. Meredith, M. Carnie, and A. Armin, *Scaling Considerations for Organic Photovoltaics for Indoor Applications*. Solar RRL, **2022**. 6(7): p. 2200315.
12. Freunek, M., M. Freunek, and L.M. Reindl, *Maximum Efficiencies of Indoor Photovoltaic Devices*. IEEE Journal of Photovoltaics, **2012**. 3(1): p. 59-64.
13. Ndiaye, A., A. Charki, A. Kobi, C.M.F. Kébé, P.A. Ndiaye, and V. Sambou, *Degradations of Silicon Photovoltaic Modules: A Literature Review*. Solar Energy, **2013**. 96: p. 140-151.
14. Ho, J.K.W., H. Yin, and S.K. So, *From 33% to 57% – An Elevated Potential of Efficiency Limit for Indoor Photovoltaics*. Journal of Materials Chemistry A, **2020**. 8(4): p. 1717-1723.
15. Shockley, W. and H.J. Queisser, *Detailed Balance Limit of Efficiency of p-n Junction Solar Cells*. Journal of Applied Physics, **1961**. 32(3): p. 510-519.

16. Nelson, J.A., *The Physics of Solar Cells*. **2003**: World Scientific Publishing Company.
17. Sprau, C., F. Buss, M. Wagner, D. Landerer, M. Koppitz, A. Schulz, D. Bahro, W. Schabel, P. Scharfer, and A. Colsmann, *Highly Efficient Polymer Solar Cells Cast from Non-Halogenated Xylene/Anisaldehyde Solution*. *Energy & Environmental Science*, **2015**. 8(9): p. 2744-2752.
18. Abbel, R., Y. Galagan, and P. Groen, *Roll-to-Roll Fabrication of Solution Processed Electronics*. *Advanced Engineering Materials*, **2018**. 20(8): p. 1701190.
19. Lee, H.K.H., Z. Li, J.R. Durrant, and W.C. Tsoi, *Is Organic Photovoltaics Promising for Indoor Applications?* *Applied Physics Letters*, **2016**. 108(25): p. 253301.
20. Lübke, D., P. Hartnagel, M. Hülsbeck, and T. Kirchartz, *Understanding the Thickness and Light-Intensity Dependent Performance of Green-Solvent Processed Organic Solar Cells*. *ACS Materials Au*, **2023**. DOI: 10.1021/acsmaterialsau.2c00070.
21. Lübke, D., P. Hartnagel, J. Angona, and T. Kirchartz, *Comparing and Quantifying Indoor Performance of Organic Solar Cells*. *Advanced Energy Materials*, **2021**. 11(34): p. 2101474.
22. Cui, Y., Y. Wang, J. Bergqvist, H. Yao, Y. Xu, B. Gao, C. Yang, S. Zhang, O. Inganäs, F. Gao, and J. Hou, *Wide-Gap Non-Fullerene Acceptor Enabling High-Performance Organic Photovoltaic Cells for Indoor Applications*. *Nature Energy*, **2019**. 4(9): p. 768-775.
23. Armin, A., W. Li, O.J. Sandberg, Z. Xiao, L. Ding, J. Nelson, D. Neher, K. Vandewal, S. Shoaei, T. Wang, H. Ade, T. Heumüller, C. Brabec, and P. Meredith, *A History and Perspective of Non-Fullerene Electron Acceptors for Organic Solar Cells*. *Advanced Energy Materials*, **2021**. 11(15): p. 2003570.
24. Hou, J., O. Inganäs, R.H. Friend, and F. Gao, *Organic Solar Cells Based on Non-Fullerene Acceptors*. *Nature Materials*, **2018**. 17(2): p. 119-128.
25. Liu, S., J. Yuan, W. Deng, M. Luo, Y. Xie, Q. Liang, Y. Zou, Z. He, H. Wu, and Y. Cao, *High-Efficiency Organic Solar Cells with Low Non-Radiative Recombination Loss and Low Energetic Disorder*. *Nature Photonics*, **2020**. 14(5): p. 300-305.
26. Colsmann, A., H. Röhm, and C. Sprau, *Shining Light on Organic Solar Cells*. *Solar RRL*, **2020**. 4(6): p. 2000015.
27. Genene, Z., W. Mammo, E. Wang, and M.R. Andersson, *Recent Advances in n-Type Polymers for All-Polymer Solar Cells*. *Advanced Materials*, **2019**. 31(22): p. 1807275.
28. Inganäs, O., *Organic Photovoltaics over Three Decades*. *Advanced Materials*, **2018**. 30(35): p. 1800388.
29. Cui, Y., L. Hong, and J. Hou, *Organic Photovoltaic Cells for Indoor Applications: Opportunities and Challenges*. *ACS Applied Materials & Interfaces*, **2020**. 12(35): p. 38815-38828.
30. Minnaert, B. and P. Veelaert, *A Proposal for Typical Artificial Light Sources for the Characterization of Indoor Photovoltaic Applications*. *Energies*, **2014**. 7(3): p. 1500-1516.
31. Hou, X., Y. Wang, H.K.H. Lee, R. Datt, N. Uslar Miano, D. Yan, M. Li, F. Zhu, B. Hou, W.C. Tsoi, and Z. Li, *Indoor Application of Emerging Photovoltaics—Progress, Challenges and Perspectives*. *Journal of Materials Chemistry A*, **2020**. 8(41): p. 21503-21525.
32. Ma, L.-K., Y. Chen, P.C.Y. Chow, G. Zhang, J. Huang, C. Ma, J. Zhang, H. Yin, A.M. Hong Cheung, K.S. Wong, S.K. So, and H. Yan, *High-Efficiency Indoor Organic Photovoltaics with a Band-Aligned Interlayer*. *Joule*, **2020**. 4(7): p. 1486-1500.
33. Zhang, Y., C. Duan, and L. Ding, *Indoor Organic Photovoltaics*. *Sci. Bull*, **2020**. 65(2040): p. 10.1016.
34. Kaiser, C., O.J. Sandberg, N. Zarrabi, W. Li, P. Meredith, and A. Armin, *A Universal Urbach Rule for Disordered Organic Semiconductors*. *Nature Communications*, **2021**. 12(1): p. 3988.
35. Hood, S., N. Zarrabi, P. Meredith, I. Kassal, and A. Armin, *Measuring Energetic Disorder in Organic Semiconductors Using the Photogenerated Charge-Separation Efficiency*. *The Journal of Physical Chemistry Letters*, **2019**. 10(14): p. 3863-3870.

36. Kay, A.M., O.J. Sandberg, N. Zarrabi, W. Li, S. Zeiske, C. Kaiser, P. Meredith, and A. Armin, *Quantifying the Excitonic Static Disorder in Organic Semiconductors*. Advanced Functional Materials, **2022**. 32(32): p. 2113181.

37. Wu, J., J. Luke, H.K.H. Lee, P. Shakya Tuladhar, H. Cha, S.-Y. Jang, W.C. Tsoi, M. Heeney, H. Kang, K. Lee, T. Kirchartz, J.-S. Kim, and J.R. Durrant, *Tail State Limited Photocurrent Collection of Thick Photoactive Layers in Organic Solar Cells*. Nature Communications, **2019**. 10(1): p. 5159.

38. Urbach, F., *The Long-Wavelength Edge of Photographic Sensitivity and of the Electronic Absorption of Solids*. Physical Review, **1953**. 92(5): p. 1324-1324.

39. Yan, J., E. Rezasoltani, M. Azzouzi, F. Eisner, and J. Nelson, *Influence of Static Disorder of Charge Transfer State on Voltage Loss in Organic Photovoltaics*. Nature Communications, **2021**. 12(1): p. 3642.

40. Beuel, S., P. Hartnagel, and T. Kirchartz, *The Influence of Photo-Induced Space Charge and Energetic Disorder on the Indoor and Outdoor Performance of Organic Solar Cells*. Advanced Theory and Simulations, **2021**. 4(3): p. 2000319.

41. Ullbrich, S., J. Benduhn, X. Jia, V.C. Nikolis, K. Tvingstedt, F. Piersimoni, S. Roland, Y. Liu, J. Wu, A. Fischer, D. Neher, S. Reineke, D. Spoltore, and K. Vandewal, *Emissive and Charge-Generating Donor–Acceptor Interfaces for Organic Optoelectronics with Low Voltage Losses*. Nature Materials, **2019**. 18(5): p. 459-464.

42. Kirchartz, T., K. Taretto, and U. Rau, *Efficiency Limits of Organic Bulk Heterojunction Solar Cells*. The Journal of Physical Chemistry C, **2009**. 113(41): p. 17958-17966.

43. Azzouzi, M., J. Yan, T. Kirchartz, K. Liu, J. Wang, H. Wu, and J. Nelson, *Nonradiative Energy Losses in Bulk-Heterojunction Organic Photovoltaics*. Physical Review X, **2018**. 8(3): p. 031055.

44. Rau, U., *Reciprocity Relation Between Photovoltaic Quantum Efficiency and Electroluminescent Emission of Solar Cells*. Physical Review B, **2007**. 76(8): p. 085303.

45. Würfel, P. and U. Würfel, *Physics of Solar Cells: From Basic Principles to Advanced Concepts*. **2016**: John Wiley & Sons.

46. Benduhn, J., K. Tvingstedt, F. Piersimoni, S. Ullbrich, Y. Fan, M. Tropiano, K.A. McGarry, O. Zeika, M.K. Riede, C.J. Douglas, S. Barlow, S.R. Marder, D. Neher, D. Spoltore, and K. Vandewal, *Intrinsic Non-Radiative Voltage Losses in Fullerene-Based Organic Solar Cells*. Nature Energy, **2017**. 2(6): p. 17053.

47. Zarrabi, N., O.J. Sandberg, S. Zeiske, W. Li, D.B. Riley, P. Meredith, and A. Armin, *Charge-Generating Mid-Gap Trap States Define the Thermodynamic Limit of Organic Photovoltaic Devices*. Nature Communications, **2020**. 11(1): p. 5567.

48. Zeiske, S., C. Kaiser, P. Meredith, and A. Armin, *Sensitivity of Sub-Bandgap External Quantum Efficiency Measurements of Solar Cells under Electrical and Light Bias*. ACS Photonics, **2020**. 7(1): p. 256-264.

49. Zeiske, S., O.J. Sandberg, N. Zarrabi, C.M. Wolff, M. Raoufi, F. Peña-Camargo, E. Gutierrez-Partida, P. Meredith, M. Stolterfoht, and A. Armin, *Static Disorder in Lead Halide Perovskites*. The Journal of Physical Chemistry Letters, **2022**. 13(31): p. 7280-7285.

50. Li, W., S. Zeiske, O.J. Sandberg, D.B. Riley, P. Meredith, and A. Armin, *Organic Solar Cells with Near-Unity Charge Generation Yield*. Energy & Environmental Science, **2021**. 14(12): p. 6484-6493.

Supporting Information

The Thermodynamic Limit of Indoor Photovoltaics Based on Energetically-Disordered Molecular Semiconductors

Austin M. Kay¹, Maura E. Fitzsimons¹, Gregory Burwell¹, Paul Meredith¹, Ardalan Armin¹, and Oskar, J. Sandberg¹

¹Sustainable Advanced Materials (Sêr-SAM), Centre for Integrative Semiconductor Materials (CISM), Department of Physics, Swansea University Bay Campus, Swansea SA1 8EN, United Kingdom

Email: ardalan.armin@swansea.ac.uk; o.j.sandberg@swansea.ac.uk

Table of Contents

Part I – Supporting Theory and Simulation Results	2
S1. Units of Illuminance	2
S2. Figures of Merit.....	4
S3. Models for Sub-Gap Absorption	8
S4. Dark Saturation Current Densities	10
S5. Deviations From the Radiative Shockley-Queisser Open-Circuit Voltage.....	14
S6. Power Conversion Efficiency Limits	17
Part II – Experimental Results and Analysis	21
S7. Material Definitions for Figure 6 of Main Text	21
S8. Methodology for Estimating Indoor Performance Using One-Sun Measurements	23
S9. Extracting Parameters from Photovoltaic External Quantum Efficiency Spectra.....	25
S10. Estimating Indoor Performance for a Variety of Systems.....	33
S11. Scaling Estimated Performance to Literature Values	35
Appendix – Dark Saturation Current Density in Organic Photovoltaics	37
References	39

Part I – Supporting Theory and Simulation Results

S1. Units of Illuminance

To provide an estimate of the upper limit of indoor photovoltaic (IPV) device performance, appropriate units should be used to describe low light intensities; these units are lux (lx) and they quantify the *illuminance* of a source. For a spectral photon flux density Φ_{source} , the illuminance (L_{source}) is defined as [1-4]

$$L_{\text{source}} = L_0 P_{\text{source}} \int_0^{\infty} V(E) \cdot E \cdot \tilde{\Phi}_{\text{source}}(E) dE = P_{\text{source}} f_{\text{source}}, \quad (\text{S1})$$

where $f_{\text{source}} = L_0 \int_0^{\infty} V(E) \cdot E \cdot \tilde{\Phi}_{\text{source}}(E) dE$ contains all the spectral information, $L_0 = 683 \text{ lx} \cdot \text{W}^{-1} \cdot \text{m}^2$ is a constant, $P_{\text{source}} = \int_0^{\infty} E \cdot \Phi_{\text{source}}(E) dE$ is the integrated irradiance of the source, and $\tilde{\Phi}_{\text{source}}$ is the spectral photon flux normalized to P_{source} . The luminous efficiency for photopic vision, $V(E)$, is plotted as a function of the photon energy (E) at a 2° viewing angle in **Figure S1a**.^[3]

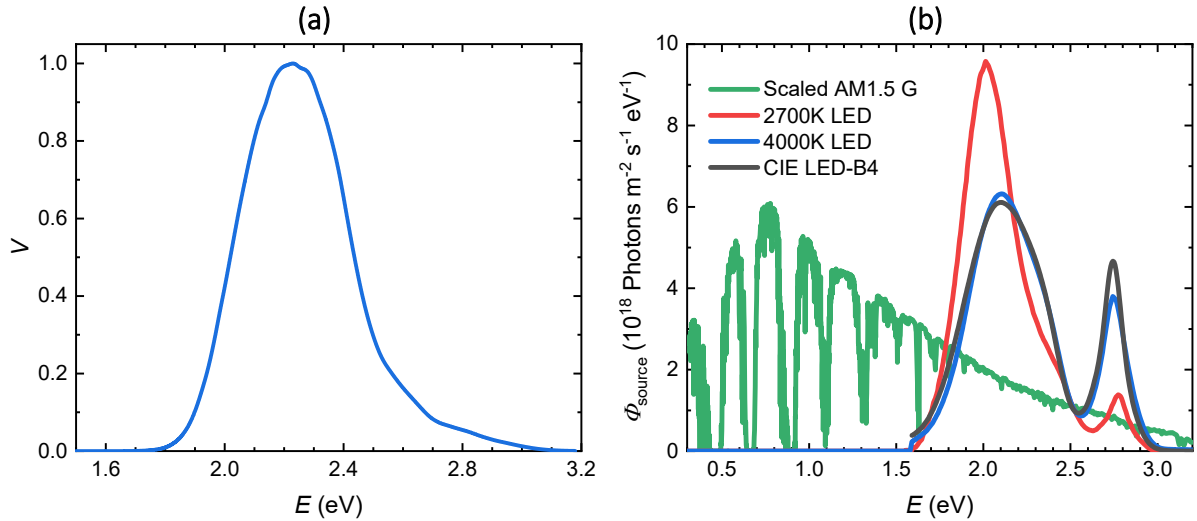


Figure S1: Converting to units of illuminance. (a) The luminous efficiency $V(E)$ for photopic vision at a 2° viewing angle, plotted as a function of the photon energy, E .^[3] (b) The spectral photon flux densities for a variety of light sources at an illuminance of 500 lux, including the AM1.5G, 2700K LED, 4000K LED, and the standard illuminant CIE LED-B4 spectra.

Using the spectral luminous efficiency of **Figure S1a**, the relationship between illuminance and irradiance was determined for the 2700K LED, the 4000K LED, standard illuminant CIE LED-B4, and AM1.5G spectra; the results are compiled in **Table S1**. Using these values, the photon fluxes associated with each of these spectra at an illuminance of 500 lux has been plotted in **Figure S1b**.

Table S1: Relationship between lux and irradiance for different spectra, determined using equation (S1) and the luminous efficiency data plotted in **Figure S1a**.

Spectrum	$f_{\text{source}} (\text{lx} \cdot \text{W}^{-1} \cdot \text{m}^2)$
AM1.5G	115.61
2700K LED	349.30
4000K LED	346.13
CIE LED B4	333.62

S2. Figures of Merit

Neglecting series and shunt resistances, the total current density generated under illumination (J_{light}) by an ideal Shockley diode (with unity ideality factor) is given by^[5, 6]

$$J_{\text{light}} = J_0 \left[\exp \left(\frac{qV_{\text{app}}}{kT} \right) - 1 \right] - J_{\text{sc}}, \quad (\text{S2})$$

where V_{app} is the voltage applied to the diode, k is the Boltzmann constant, T is the temperature, $J_{\text{sc}} = q \int_0^{\infty} \text{EQE}_{\text{PV}}(E) \Phi_{\text{source}}(E) dE$ is the short-circuit current density under illumination, and $J_0 = \frac{q}{\text{EQE}_{\text{EL}}} \int_0^{\infty} \text{EQE}_{\text{PV}}(E) \Phi_{\text{bb}}(E) dE$ is the dark saturation current density. In these expressions, q denotes the elementary charge, Φ_{bb} is the spectral photon flux associated with a black body at temperature T , and EQE_{PV} and EQE_{EL} are the photovoltaic and electroluminescent external quantum efficiencies, respectively.

At open-circuit conditions, where the applied voltage is equal to the open-circuit voltage (V_{oc}), no net current is produced by the device. Rearranging Equation (S2) in this case yields

$$V_{\text{oc}} = \frac{kT}{q} \ln \left[1 + \frac{J_{\text{sc}}}{J_0} \right]. \quad (\text{S3})$$

To calculate the power conversion efficiency (PCE), the power outputted by the device at the maximum power point (V_{mpp}) must be determined. This is done by first multiplying Equation (S2) with V_{app} to find the power density. Following this, taking the derivative with respect to the applied voltage, setting the whole expression equal to nought, and rearranging gives $\exp \left(1 + \frac{qV_{\text{oc}}}{kT} \right) = \left(1 + \frac{qV_{\text{mpp}}}{kT} \right) \exp \left(1 + \frac{qV_{\text{mpp}}}{kT} \right)$, which was solved in this work using the Lambert W function, as seen in other works in the literature.^[7-10] The maximum power point voltage then relates to V_{oc} via

$$V_{\text{mpp}} = \frac{kT}{q} \left(W \left[\exp \left(1 + \frac{qV_{\text{oc}}}{kT} \right) \right] - 1 \right). \quad (\text{S4})$$

The solar cell's fill factor (FF) was then determined using:

$$FF = \frac{|J_{mpp}|V_{mpp}}{J_{sc}V_{oc}}, \quad (S5)$$

where the current density at the maximum power point (J_{mpp}) is determined by substituting V_{mpp} , determined using Equation (S4), back into Equation (S2).

A free-standing expression for the fill factor in terms of the open-circuit voltage can be obtained from Equations (S1) to (S5) using Newton's method to approximate the Lambert W function (in the large-argument limit), yielding^[11]

$$W[x] \approx \ln(x) \left(1 - \frac{\ln[\ln(x)]}{1 + \ln[x]} \right). \quad (S6)$$

Consequently, the maximum power point voltage can be written in terms of the open-circuit voltage as

$$V_{mpp} \approx V_{oc} \left[1 - \frac{kT}{qV_{oc}} \left(\frac{1 + \frac{qV_{oc}}{kT}}{2 + \frac{qV_{oc}}{kT}} \right) \ln \left[1 + \frac{qV_{oc}}{kT} \right] \right]. \quad (S7)$$

Whereas the photocurrent density at the maximum power point in terms of the open-circuit voltage is, with

$$\frac{J_0}{J_{sc}} = \left[\exp \left(\frac{qV_{oc}}{kT} \right) - 1 \right]^{-1},$$

$$J_{mpp} = J_{sc} \left[\exp \left(- \left[\frac{1 + \frac{qV_{oc}}{kT}}{2 + \frac{qV_{oc}}{kT}} \right] \ln \left[1 + \frac{qV_{oc}}{kT} \right] \right) - 1 \right] \left[1 - \exp \left(- \frac{qV_{oc}}{kT} \right) \right]^{-1}. \quad (S8)$$

The fill factor can then be written as

$$FF \approx \frac{\left[1 - \frac{kT}{qV_{oc}} \left(\frac{1 + \frac{qV_{oc}}{kT}}{2 + \frac{qV_{oc}}{kT}} \right) \ln \left[1 + \frac{qV_{oc}}{kT} \right] \right] \left[1 - \exp \left(- \left[\frac{1 + \frac{qV_{oc}}{kT}}{2 + \frac{qV_{oc}}{kT}} \right] \ln \left[1 + \frac{qV_{oc}}{kT} \right] \right) \right]}{1 - \exp \left(- \frac{qV_{oc}}{kT} \right)}. \quad (S9)$$

For open-circuit voltages larger than around 0.2 V, this reduces to

$$FF \approx \left[1 - \frac{kT}{qV_{oc}} \left(\frac{1 + \frac{qV_{oc}}{kT}}{2 + \frac{qV_{oc}}{kT}} \right) \ln \left[1 + \frac{qV_{oc}}{kT} \right] \right] \left[1 - \exp \left(- \left[\frac{1 + \frac{qV_{oc}}{kT}}{2 + \frac{qV_{oc}}{kT}} \right] \ln \left[1 + \frac{qV_{oc}}{kT} \right] \right) \right]. \quad (\text{S10})$$

In the further limit that the open-circuit voltage is greater than around 0.5 V, Equation **(S10)** can be further simplified to give

$$FF \approx \frac{\frac{qV_{oc}}{kT} - \ln \left(1 + \frac{qV_{oc}}{kT} \right)}{1 + \frac{qV_{oc}}{kT}}. \quad (\text{S11})$$

This expression for the fill factor is the same as in Würfel's *Physics of Solar Cells*.^[12] In the remainder of this work (and in the computational tool we provide as **Supporting Material**), we calculate the fill factor through the maximum power point voltage given by Equation **(S4)** and the current density at the maximum power point, which is determined by substituting $V_{app} = V_{mpp}$ into Equation **(S2)**. By doing this, we can more readily compute the maximum power point parameters, which is ideal as they are more pertinent for indoor applications than figures-of-merit like the fill factor and the power conversion efficiency. We stress that Equation **(S11)** is valid for the open-circuit voltages of most working solar cells, and most indoor photovoltaics.

S3. Models for Sub-Gap Absorption

In the main text, different models for EQE_{PV} are considered. The first of these is a rudimentary step function, where photons of greater than the optical gap (E_{opt}) generate an electron-hole pair with efficiency EQE_{max} , while photons of energy less than the optical gap do not:

$$\text{EQE}_{\text{PV}}(E) = \begin{cases} \text{EQE}_{\text{max}}, & \text{if } E \geq E_{\text{opt}}, \\ 0, & \text{otherwise.} \end{cases} \quad (\text{S12})$$

In the second model, previously proposed to describe excitonic sub-gap absorption for organic photovoltaics (OPVs) by the authors, the EQE_{PV} is given by^[13, 14]

$$\text{EQE}_{\text{PV}}(E) = \frac{\text{EQE}_{\text{max}}}{2} \left\{ \exp \left[\frac{E - E_{\text{opt}} + \frac{\sigma_s^2}{2kT}}{kT} \right] \text{erfc} \left[\frac{E - E_{\text{opt}} + \frac{\sigma_s^2}{kT}}{\sigma_s \sqrt{2}} \right] + \text{erfc} \left[\frac{E_{\text{opt}} - E}{\sigma_s \sqrt{2}} \right] \right\}. \quad (\text{S13})$$

Here, E_{opt} is the mean optical gap of a Gaussian distribution of exciton states with standard σ_s – the excitonic static disorder. In this expression, erfc denotes the complementary error function.^[15] The third model for EQE_{PV} which will be considered can be thought of as being halfway between the step function model of Equation (S12) and the disorder-dependent EQE_{PV} model given by Equation (S13). It combines an above-gap quantum efficiency EQE_{max} with a sub-gap Urbach tail characterized with Urbach energy E_U , give^[16]

$$\text{EQE}_{\text{PV}}(E) = \text{EQE}_{\text{max}} \left\{ \begin{array}{ll} 1, & \text{if } E \geq E_{\text{opt}}, \\ \exp \left(\frac{E - E_{\text{opt}}}{E_U} \right), & \text{otherwise.} \end{array} \right. \quad (\text{S14})$$

The spectral behavior of Equation (S13) and Equation (S14) are plotted in **Figure S2a** and **S2b**, respectively.

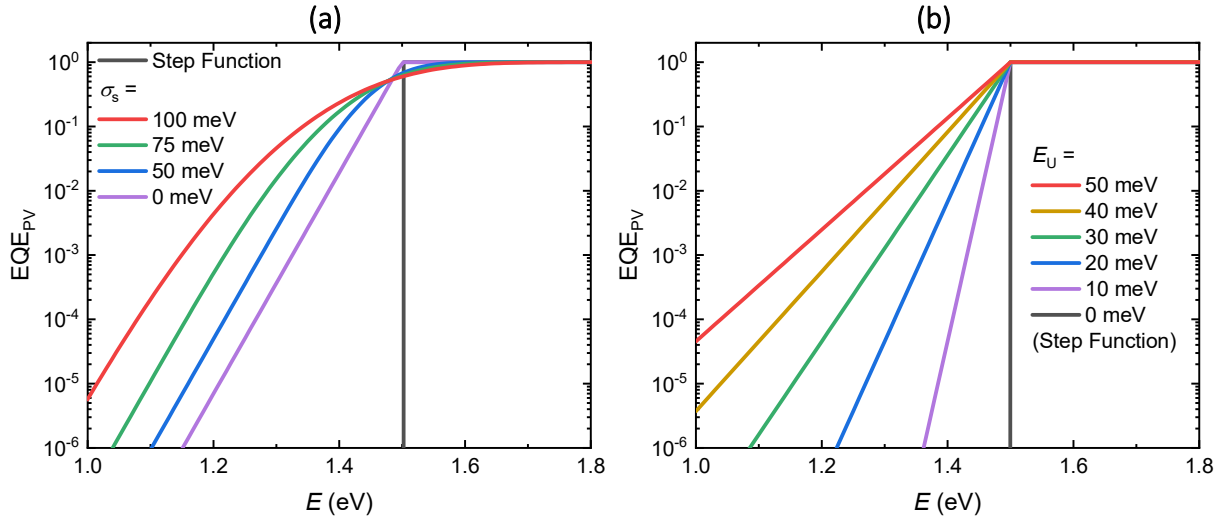


Figure S2: Models for the sub-gap photovoltaic external quantum efficiency for $E_{\text{opt}} = 1.5$ eV. **(a)** EQE_{PV} determined using Equation (S13) for a variety of σ_s and compared with the step function model determined using Equation (S12). **(b)** EQE_{PV} in the sub-gap Urbach tail model, for a variety of E_U , determined using Equation (S14). The $E_U = 0$ case is equivalent to the step function model.

From **Figure S2**, it is clear that sub-gap Urbach tails with larger E_U have increased sub-gap absorption. The band edges of systems with smaller Urbach energies, like perovskites, are therefore much better defined than the band edges of non-crystalline semiconductors.^[17] Using these models for EQE_{PV} spectra, the dark saturation current densities in the radiative limit (and the consequent open-circuit voltages and power conversion efficiencies) are calculated in the next section.

S4. Dark Saturation Current Densities

The dark saturation current density in the radiative limit (J_0^{rad}) is determined using the black-body photon flux density, which itself is given by ^[5, 18, 19]

$$\Phi_{\text{bb}}(E) = \frac{2\pi E^2}{h^3 c^2} \frac{1}{\exp\left(\frac{E}{kT}\right) - 1}. \quad (\text{S15})$$

Here, h is the Planck constant and c is the speed of light. Using Equation (S15), with the Fermi-Dirac distribution being approximated by the Maxwell-Boltzmann distribution, the dark saturation current in the radiative limit is given by

$$J_0^{\text{rad}} \approx \frac{2\pi q}{h^3 c^2} \int_0^{\infty} \text{QE}_{\text{PV}}(E) E^2 \exp\left(-\frac{E}{kT}\right) dE, \quad (\text{S16})$$

where the Bose-Einstein distribution has been approximated as the Maxwell-Boltzmann distribution to alleviate the evaluation of the integrals; this approximation is valid for $E > 2kT$. ^[12]

The radiative dark saturation current density in the step-function QE_{PV} model will be given by substituting Equation (S12) into Equation (S16) and using the definition of the gamma function, $\Gamma(n + 1) = \int_0^{\infty} x^n e^{-x} dx = n!$, giving ^[15]

$$J_0^{\text{rad}} \approx \frac{2\pi q \text{QE}_{\text{max}}}{h^3 c^2} [2k^3 T^3 + 2E_{\text{opt}} k^2 T^2 + E_{\text{opt}}^2 kT] \exp\left(-\frac{E_{\text{opt}}}{kT}\right). \quad (\text{S17})$$

The approximation that $E_{\text{opt}} \gg kT$ may be made to simplify Equation (S17), but, for now, this approximation is not made. On the other hand, it is shown in the **Appendix** that, by substituting Equation (S13) into Equation (S16), the radiative dark saturation current density is given by

$$J_0^{\text{rad}} = \frac{\pi q \text{QE}_{\text{max}}}{h^3 c^2} \left[f_1 \exp\left(-\frac{\Delta^2}{2\sigma_s^2}\right) + f_2 \text{erfc}\left(\frac{\Delta}{\sigma_s \sqrt{2}}\right) \right] \exp\left(\frac{-E_{\text{opt}} + \frac{\sigma_s^2}{2kT}}{kT}\right). \quad (\text{S18})$$

Where the parameters Δ , f_1 , and f_2 are defined as

$$\Delta = -E_{\text{opt}} + \frac{\sigma_s^2}{kT} \quad (\text{S19a})$$

$$f_1 = \sigma_s \sqrt{\frac{2}{\pi} \left(\frac{\Delta^2 + 2\sigma_s^2}{3} - \Delta kT + 2k^2 T^2 \right)}, \quad (\text{S19b})$$

$$f_2 = (\Delta^2 + \sigma_s^2)kT - \Delta(2k^2 T^2 + \sigma_s^2) + 2k^3 T^3 - \frac{\Delta^3}{3}. \quad (\text{S19c})$$

In the limit that $E_{\text{opt}} \gg \sigma_s$, the exponential term decays rapidly and the complementary error function term tends to a constant value of two, giving

$$\begin{aligned} J_0^{\text{rad}} \Big|_{E_{\text{opt}} \gg \sigma_s} &\approx \frac{2\pi q \text{QE}_{\text{max}} f_2}{h^3 c^2} \exp\left(\frac{-E_{\text{opt}} + \frac{\sigma_s^2}{2kT}}{kT}\right) \\ &\approx \left(E_{\text{opt}} - \frac{\sigma_s^2}{kT}\right)^3 \frac{2\pi q \text{QE}_{\text{max}}}{3h^3 c^2} \exp\left(\frac{-E_{\text{opt}} + \frac{\sigma_s^2}{2kT}}{kT}\right). \end{aligned} \quad (\text{S20})$$

In the sub-gap Urbach tail model, QE_{PV} is instead modelled using Equation (S14), giving the following radiative dark saturation current density

$$\begin{aligned} J_0^{\text{rad}} &\approx \frac{2\pi q \text{QE}_{\text{max}}}{h^3 c^2} \left\{ \left[\frac{2}{m^3} - \left(\frac{E_{\text{opt}}^2}{m} + \frac{2E_{\text{opt}}}{m^2} + \frac{2}{m^3} \right) e^{-mE_{\text{opt}}} \right] \exp\left(-\frac{E_{\text{opt}}}{E_{\text{U}}}\right) \right. \\ &\quad \left. + \left[2k^3 T^3 + 2E_{\text{opt}} k^2 T^2 + E_{\text{opt}}^2 kT \right] \exp\left(-\frac{E_{\text{opt}}}{kT}\right) \right\}, \end{aligned} \quad (\text{S21})$$

where $m = \frac{1}{kT} - \frac{1}{E_{\text{U}}}$. Equation (S21) is valid only for $E_{\text{U}} \neq kT$, i.e., for $m \neq 0$. In the special case that $E_{\text{U}} = kT$, one finds

$$J_0^{\text{rad},*} \approx \frac{2\pi q \text{QE}_{\text{max}}}{h^3 c^2} \left[2k^3 T^3 + 2E_{\text{opt}} k^2 T^2 + E_{\text{opt}}^2 kT + \frac{E_{\text{opt}}^3}{3} \right] \exp\left(-\frac{E_{\text{opt}}}{kT}\right). \quad (\text{S22})$$

Both the OPV and sub-gap Urbach tail models for QE_{PV} include additional contributions to the dark saturation current density, which are not present in the simple step function model. As illustrated by the simulated dark saturation current densities of Figure S3, these contributions result in orders of magnitude

increases. Furthermore, increasing the excitonic disorder σ_s is shown to also increase the dark saturation current density, but have little effect on the gradient of the line as a function of E_{opt} . On the other hand, increasing E_U beyond 20 meV results in vast increases in J_0^{rad} , with the gradients of the curves depending on E_U . In panels **a** and **b** of **Figure S3**, it is shown that the short-circuit current density is mostly unperturbed by changes in σ_s and E_U , whereas variations in the dark saturation current density are by orders of magnitude.

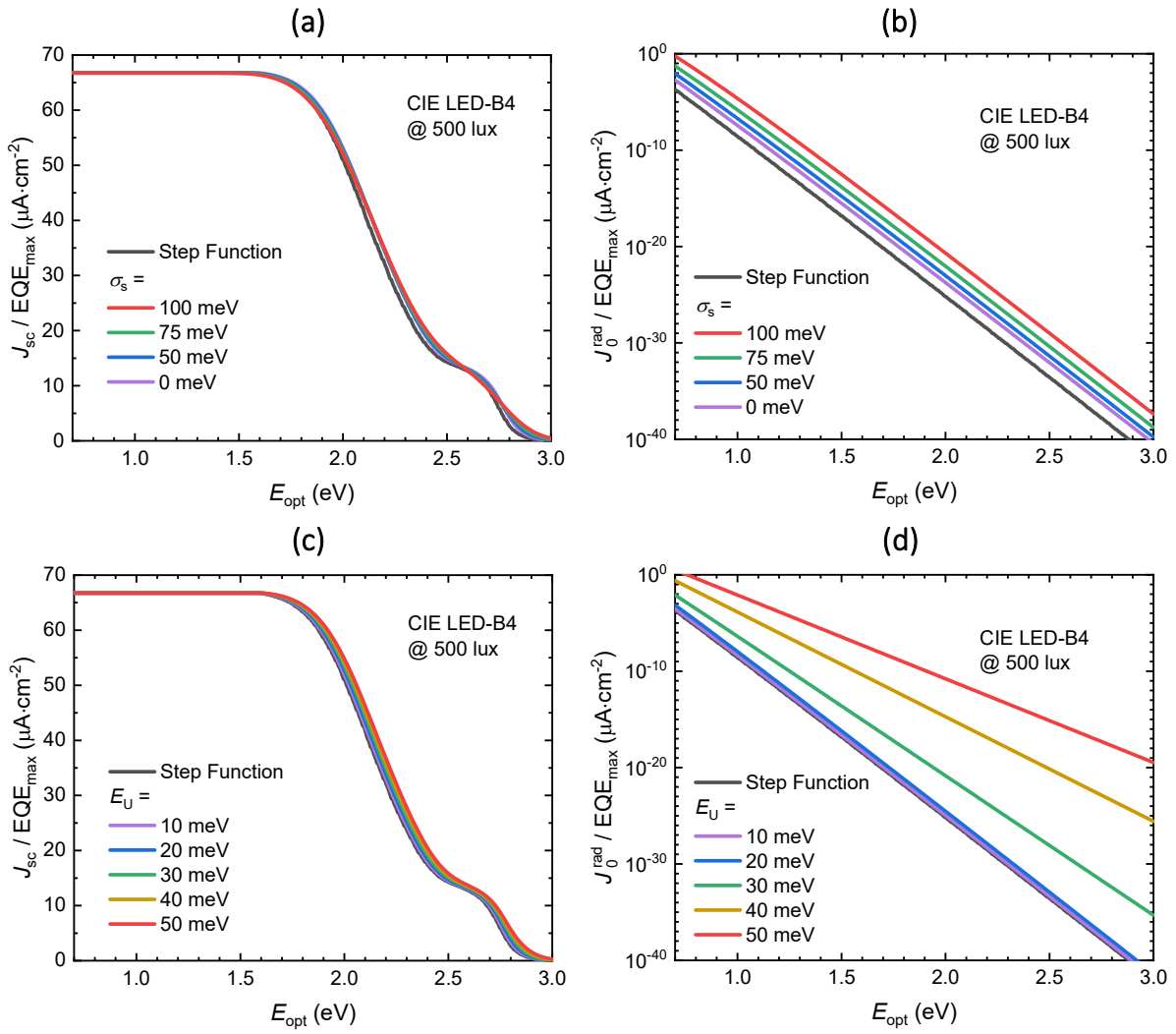


Figure S3: Simulated current densities under the CIE LED-B4 spectrum at 500 lux, normalized to the above-gap photovoltaic quantum efficiency, EQE_{max} . **(a)** The short-circuit current density and **(b)** the

radiative dark saturation current density, both as a function of the optical gap for σ_s varied from 0 to 100 meV. These curves were simulated using an EQE_{PV} spectrum modelled by Equation **(S13)**, which was substituted into $J_{sc} = q \int_0^{\infty} \text{EQE}_{\text{PV}}(E) \Phi_{\text{source}}(E) dE$ and $J_0^{\text{rad}} = q \int_0^{\infty} \text{EQE}_{\text{PV}}(E) \Phi_{\text{bb}}(E) dE$, respectively. Alternatively, in **(c)** and **(d)**, the short-circuit current density and radiative dark saturation current density was simulated using an EQE_{PV} modelled by Equation **(S14)**, where E_U has been varied from 0 to 50 meV.

S5. Deviations From the Radiative Shockley-Queisser Open-Circuit Voltage

The radiative open-circuit voltage loss induced by sub-gap absorption was taken as the deviation between the Shockley-Queisser (SQ) open-circuit voltage ($V_{\text{oc}}^{\text{SQ}}$) and the obtained radiative open-circuit voltage ($V_{\text{oc}}^{\text{rad}}$)

$$\Delta V_{\text{oc,sub-gap}}^{\text{rad}} = V_{\text{oc}}^{\text{SQ}} - V_{\text{oc}}^{\text{rad}}. \quad (\text{S23})$$

As demonstrated by **Figure S3** in the previous section, regardless of the amount of sub-gap absorption that is present, the short-circuit current density is roughly the same. We therefore assume that $J_{\text{sc}} \approx J_{\text{sc}}^{\text{SQ}} = q \int_{E_{\text{opt}}}^{\infty} \Phi_{\text{source}}(E) dE$. The dark saturation current density, however, is strongly dependent on the absorption parameters. By combining Equation (S23), with Equation (S3), one may write the deviation from $V_{\text{oc}}^{\text{SQ}}$ in the radiative limit ($\text{EQE}_{\text{EL}} = 1$) as

$$\Delta V_{\text{oc,sub-gap}}^{\text{rad}} = \frac{kT}{q} \ln \left[\frac{J_0^{\text{rad}}}{J_0^{\text{rad,SQ}}} \frac{J_0^{\text{rad,SQ}} + J_{\text{sc}}^{\text{SQ}}}{J_0^{\text{rad}} + J_{\text{sc}}} \right] \approx \frac{kT}{q} \ln \left[\frac{J_0^{\text{rad}}}{J_0^{\text{rad,SQ}}} \frac{J_0^{\text{rad,SQ}} + J_{\text{sc}}^{\text{SQ}}}{J_0^{\text{rad}} + J_{\text{sc}}^{\text{SQ}}} \right]. \quad (\text{S24})$$

In the limit that $J_{\text{sc}}^{\text{SQ}} \gg J_0^{\text{SQ}}$ and $J_{\text{sc}}^{\text{SQ}} \gg J_0^{\text{rad}}$, which, as highlighted by **Figure S3**, can safely be assumed for $E_{\text{opt}} > 1.0$ eV, Equation (S24) reduces to $\Delta V_{\text{oc,sub-gap}}^{\text{rad}} \approx \frac{kT}{q} \ln \left[\frac{J_0^{\text{rad}}}{J_0^{\text{rad,SQ}}} \right]$. Substituting in the dark saturation current density given by Equation (S18), the radiative open-circuit voltage loss induced by sub-gap absorption can be written as

$$\Delta V_{\text{oc,sub-gap}}^{\text{rad}} \approx \frac{\sigma_s^2}{2qkT} + \frac{kT}{q} \ln \left[\frac{f_1 \exp \left(-\frac{\Delta^2}{2\sigma_s^2} \right) + f_2 \operatorname{erfc} \left(\frac{\Delta}{\sigma_s \sqrt{2}} \right)}{4(kT)^3 + 4E_{\text{opt}}(kT)^2 + 2E_{\text{opt}}^2(kT)} \right]. \quad (\text{S25})$$

The parameters Δ , f_1 , and f_2 were defined in Equation (S19). Making use of the approximations that arise when $E_{\text{opt}} \gg \sigma_s$ and $E_{\text{opt}} \gg kT$, this expression reduces to

$$\Delta V_{\text{oc,sub-gap}}^{\text{rad}} \approx \frac{\sigma_s^2}{2qkT} + \frac{kT}{q} \ln \left[\frac{E_{\text{opt}}}{3kT} \left(1 - \frac{\sigma_s^2}{E_{\text{opt}}kT} \right)^3 \right]. \quad (\text{S26})$$

This behavior of this expression as a function of E_{opt} is explored for a variety of σ_s values in **Figure 3c** of the main text.

On the other hand, the radiative open-circuit voltage losses induced by sub-gap absorption in the Urbach tail model is determined by substituting Equation (S21) into $\Delta V_{\text{oc,sub-g}}^{\text{rad}} \approx \frac{kT}{q} \ln \left[\frac{J_0^{\text{rad}}}{J_0^{\text{rad,SQ}}} \right]$, giving

$$\Delta V_{\text{oc,sub-gap}}^{\text{rad}} \approx \frac{kT}{q} \ln \left[\frac{\frac{2}{m^3} (e^{mE_{\text{opt}}} - 1) - \frac{E_{\text{opt}}^2}{m} - \frac{2E_{\text{opt}}}{m^2}}{E_{\text{opt}}^2 kT} + 1 \right], \quad (\text{S27})$$

where $E_{\text{opt}} \gg kT$ has been assumed and the parameter m is defined by $m = \frac{1}{kT} - \frac{1}{E_U}$ as before. In the limit that $E_U = kT$, expanding the exponential term of Equation (S27) gives

$$\Delta V_{\text{oc,sub-gap}}^{\text{rad}} \approx \frac{kT}{q} \ln \left[\frac{E_{\text{opt}}}{3kT} + 1 \right]. \quad (\text{S28})$$

Whereas, in the limit that $E_U > kT$, Equation (S27) may be approximated as

$$\Delta V_{\text{oc,sub-gap}}^{\text{rad}} \approx \frac{E_{\text{opt}}}{q} \left(1 - \frac{kT}{E_U} \right) + \frac{kT}{q} \ln \left[\frac{2(kT)^2}{E_{\text{opt}}^2 \left(1 - \frac{kT}{E_U} \right)^3} \right]. \quad (\text{S29})$$

At room temperature, Equation (S29) will not accurately predict open-circuit voltage losses induced by sub-gap absorption for $E_U < 30$ meV; it is therefore not applicable to crystalline semiconductors or perovskites and Equation (S27) should be used instead. The behavior of Equation (S27) is plotted for a variety of E_U values as dashed lines in **Figure S4**. Therein, the deviation from $V_{\text{oc}}^{\text{SQ}}$ induced by sub-gap absorption has also been determined numerically and plotted as colored lines. From this graph, it is evident that Urbach tails with $E_U < 20$ meV result in far less open-circuit voltage loss than those with $E_U \geq 30$ meV.

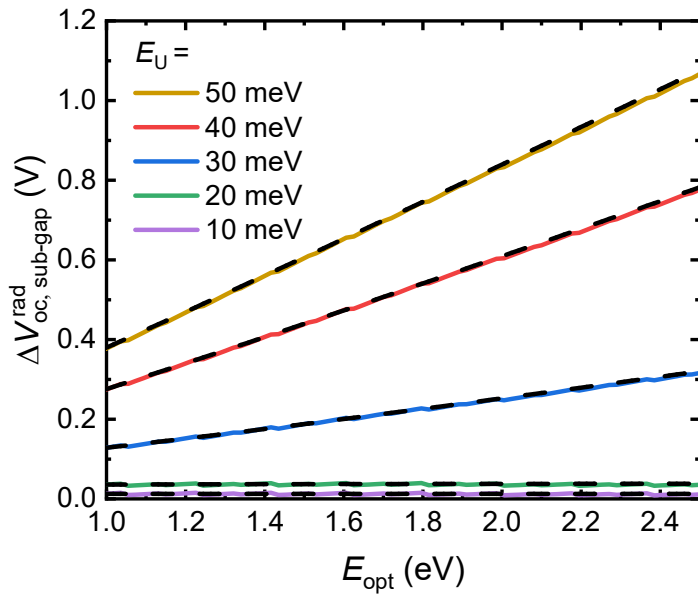


Figure S4: Deviations from the radiative open-circuit voltage in the SQ model induced by the absorption of sub-gap Urbach tails with Urbach energy E_U ranging from 10 meV to 50 meV. The solid, coloured lines were calculated numerically, whereas the dashed lines indicate the approximation given by Equation (S27).

S6. Power Conversion Efficiency Limits

By combining all the theory outlined in **Sections S1-S5**, the power conversion efficiency could be simulated in the radiative limit for the EQE_{PV} models based on Equation **(S14)** (for a variety of Urbach energies) and Equation **(S13)** (for a variety of σ_s) – the results are illustrated for the former in **Figure S5**, and for the latter in **Figure S6**. In **panel a** of those figures, the PCE is plotted as a function of the optical gap under the CIE LED-B4 spectrum at 500 lux. Whereas, in **panel b** of those figures, the maximum PCE is plotted as a function of the illuminance; the optical gaps that produce the maximum PCEs in the Urbach tail model are provided in **Table S2**, whereas the corresponding optical gaps for the EQE_{PV} model based on Equation **(S13)** are summarized in **Table S3**.

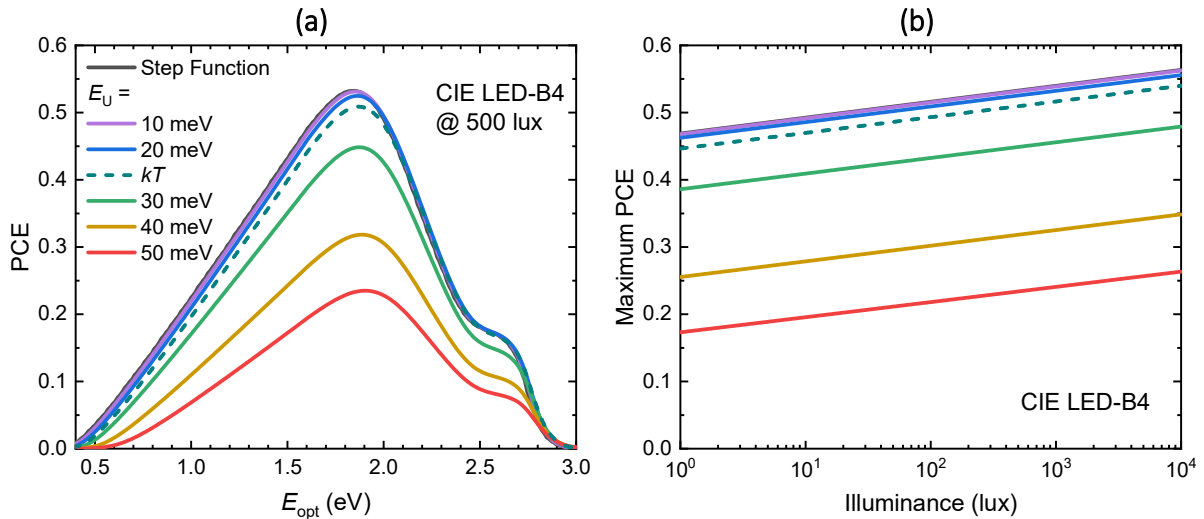


Figure S5: Power conversion efficiency in the radiative limit under CIE LED-B4 illumination for a variety of Urbach energies. **(a)** PCE versus optical gap at 500 lux. **(b)** Maximum PCE versus illuminance, with the highest-performing E_{opt} values summarised in **Table S2**. The $E_U = 0$ case is equivalent to a step-function EQE_{PV} . The $E_U = kT$ case is indicated by the dashed line.

From **Figure S5**, one can see that sub-gap tails with Urbach energies less than 20 meV induce such little open-circuit voltage losses that the PCE in the radiative limit is essentially the same as the SQ model. For Urbach energies greater than 20 meV, however, the losses become more considerable. Consequently,

the PCE drops by around 3% from the SQ model value when a sub-gap tail with $E_U = kT$ is included (at room temperature, $T = 293.15$ K), as illustrated by the dashed line. Comparing these Urbach energy-dependent results with the energetic disorder-dependent results of **Figure S6**, one can see that a large E_U on the order of 50 meV is far more detrimental to the PCE in the thermodynamic limit than a large energetic disorder on the order of 100 meV. However, higher levels of energetic disorder still thermodynamically constrain the PCE more than lower levels of energetic disorder.

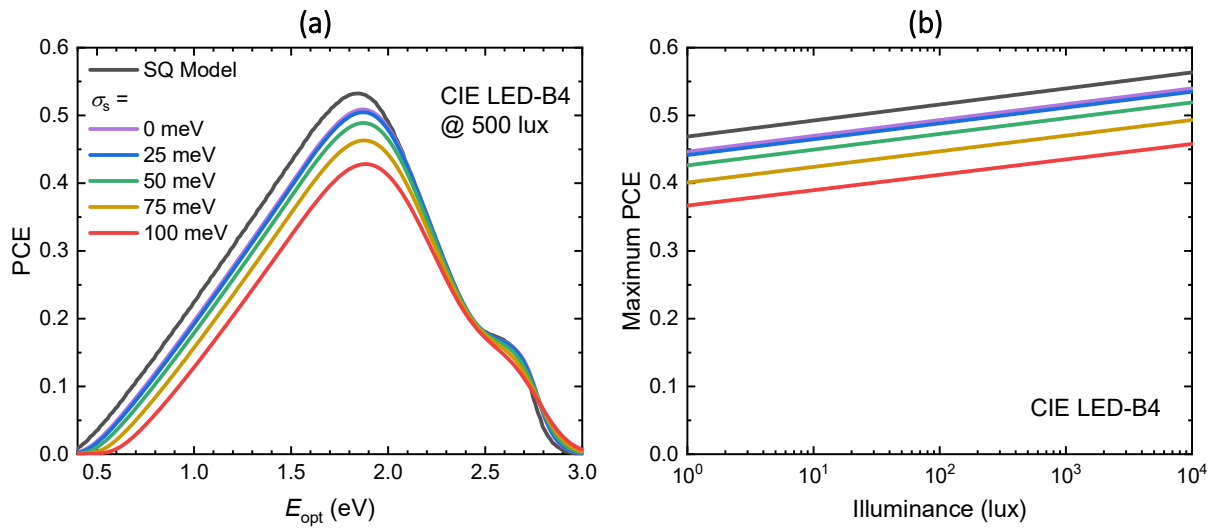


Figure S6: Power conversion efficiency in the radiative limit under CIE LED-B4 illumination for a variety of excitonic static disorder σ_s . **(a)** PCE versus optical gap at 500 lux. **(b)** Maximum PCE versus illuminance, with the highest-performing E_{opt} values summarised in **Table S3**. The SQ model has also been illustrated by the black curves.

In **Figure 5** of the main text, the PCE of IPVs has been simulated under the CIE LED-B4 standard illuminant. These PCEs have also been simulated under illumination by the ‘warm white’ 2700K LED and ‘cool white’ 4000K LED spectra with the results being plotted in **Figure S7**. We note that similar results are obtained to the ones described in the main text for CIE LED-B4.

Table S2: The optical gaps that produce the maximum PCEs illustrated in **Figure S5b**, provided alongside the Urbach energies that describe the curve.

Urbach Energy, E_U (meV)	Best Optical Gap (eV)
0 (SQ Model)	1.83018
10	1.84582
20	1.87753
$kT = 25.26$	1.87754
30	1.87754
40	1.87754
50	1.90979

Table S3: The optical gaps that produce the maximum PCEs illustrated in **Figure S6b**, provided alongside the excitonic static disorder values that describe the curve.

Excitonic Static Disorder, σ_s (meV)	Best Optical Gap (eV)
SQ Model	1.83018
0	1.87754
25	1.86933
50	1.87485
75	1.87382
100	1.87992

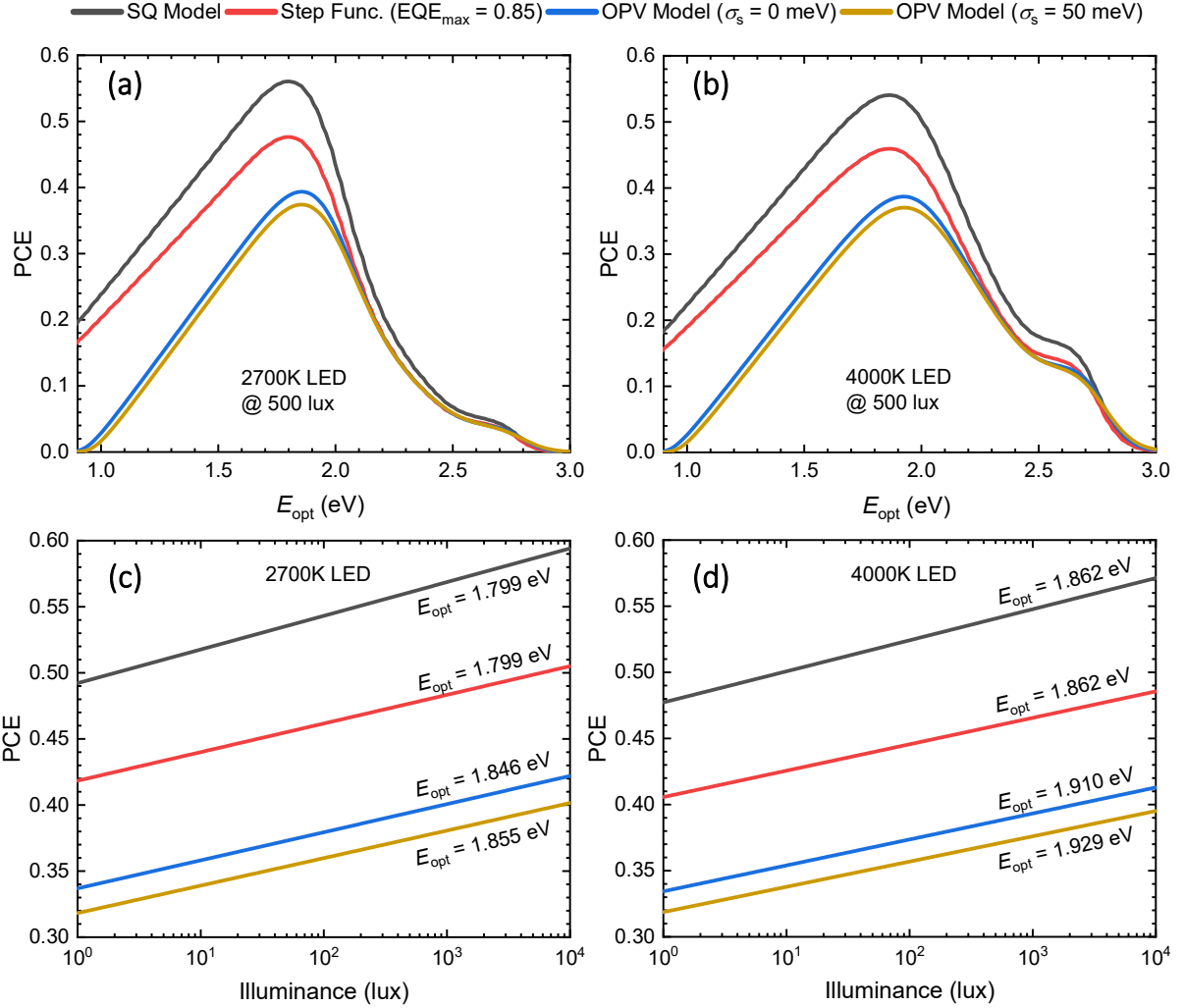


Figure S7: Power conversion efficiency in the SQ model (black), in the step function case determined using a step function with $\text{EQE}_{\text{max}} = 0.85$, and in a realistic OPV limit for both the $\sigma_s = 0$ meV case (blue) and the $\sigma_s = 50$ meV case (yellow). The latter is determined using a combination of the OPV model for the EQE_{PV} and the realistic non-radiative open-circuit voltage model described in the main text. (a) and (b) show the PCE versus optical gap at an illuminance of 500 lux for the 2700K LED and the 4000K LED, respectively. Whereas (c) and (d) show the PCE versus illuminance for the best-performing optical gap (inset with the curves), for the 2700K LED and 4000K LED, respectively.

Part II – Experimental Results and Analysis

S7. Material Definitions for Figure 6 of Main Text

BQR: N~2~-[7-(3,4-dimethoxyphenyl)quinoxalin-2-yl]-N-methylglycinamide

BTP-eC9: 2,2'-[[12,13-Bis(2-butyloctyl)-12,13-dihydro-3,9-dinonylbisthieno[2",3":4',5']thieno[2',3':4,5]pyrrolo[3,2-e:2',3'-g][2,1,3]benzothiadiazole-2,10-diy]bis[methylidyne(5,6-chloro-3-oxo-1H-indene-2,1(3H)-diylidene)]]bis[propanedinitrile]

EH-IDTBR: (5Z)-3-ethyl-2-sulfanylidene-5-[[4-[9,9,18,18-tetrakis(2-ethylhexyl)-15-[7-[(Z)-(3-ethyl-4-oxo-2-sulfanylidene1,3-thiazolidin-5-ylidene)methyl]-2,1,3-benzothiadiazol-4-yl]-5,14-dithiapentacyclo[10.6.0.03,10.04,8.013,17]octadeca-1(12),2,4(8),6,10,13(17),15-heptaen-6-yl]-2,1,3-benzothiadiazol-7-yl]methylidene]-1,3-thiazolidin-4-one

ITIC: 3,9-bis(2-methylene-(3-(1,1-dicyanomethylene)-indanone))-5,5,11,11-tetrakis(4-hexylphenyl)-dithieno[2,3-d:2',3'-d']-s-indaceno[1,2-b:5,6-b']dithiophene

O-IDTBR: (5Z,5'Z)-5,5'-((7,7'-(4,4,9,9-tetraoctyl-4,9-dihydro-s-indaceno[1,2-b:5,6-b']dithiophene-2,7-diy)bis(benzo[c][1,2,5]thiadiazole-7,4-diy))bis(methanlylylidene))bis(3-ethyl-2-thioxothiazolidin-4-one)

PBDB-T: Poly[(2,6-(4,8-bis(5-(2-ethylhexyl)thiophen-2-yl)-benzo[1,2-b:4,5-b']dithiophene))-alt-(5,5-(1',3'-di-2-thienyl-5',7'-bis(2-ethylhexyl)benzo[1',2'-c:4',5'-c']dithiophene-4,8-dione)]

PC₇₁BM: [6,6]-phenyl-C₇₁-butyric acid methyl ester

PDINO: 2,9-bis[3-(dimethyloxidoamino)propyl]anthra[2,1,9-def:6,5,10-d'e'f']diisoquinoline-1,3,8,10(2H,9H)-tetrone

PEDOT:PSS: Poly(3,4-ethylenedioxythiophene) polystyrene sulfonat

PM6: Poly[(2,6-(4,8-bis(5-(2-ethylhexyl-3-fluoro)thiophen-2-yl)-benzo[1,2-b:4,5-b']dithiophene))-alt-(5,5-(1',3'-di-2-thienyl-5',7'-bis(2-ethylhexyl)benzo[1',2'-c:4',5'-c']dithiophene-4,8-dione)]

Y6: 2,2'-(*Z,Z*)-((12,13-bis(2-ethylhexyl)-3,9-diundecyl-12,13-dihydro-[1,2,5]thiadiazolo[3,4-*e*]thieno[2'',3'':4',5']thieno[2',3':4,5]pyrrolo[3,2-*g*]thieno[2',3':4,5]thieno[3,2-*b*]indole-2,10-diylyl)bis(methanoylylidene))bis(5,6-difluoro-3-oxo-2,3-dihydro-1*H*-indene-2,1-diylyl)dimalononitrile

Crystalline Silicon: Commercial crystalline silicon solar cell (Part number: KXOB22-12X1)

Amorphous Silicon: a-Si:H thin-film solar cell made by Trony (SC80125s-8)

S8. Methodology for Estimating Indoor Performance Using One-Sun Measurements

To make realistic predictions for the figures-of-merit of photovoltaic materials in indoor settings, we devised a methodology that takes experimentally-determined measurements of the photovoltaic external quantum efficiency and the open-circuit voltage under one-Sun conditions (V_{oc}^{\odot}) as inputs. As illustrated by the left-hand ‘AM1.5 Global Conditions’ pane of the block diagram in **Figure S8**, V_{oc}^{\odot} can be determined from a device’s current-voltage curve. The EQE_{PV} spectrum, on the other hand, can be used to determine the short-circuit and dark saturations current densities using

$$J_{\text{sc}} = q \int_{E_{\text{lower}}}^{\infty} \text{EQE}_{\text{PV}}(E) \Phi_{\text{source}}(E) \, dE \quad (\text{S30a})$$

$$J_0^{\text{rad}} = q \int_{E_{\text{lower}}}^{\infty} \text{EQE}_{\text{PV}}(E) \Phi_{\text{bb}}(E) \, dE. \quad (\text{S30b})$$

Here, E_{lower} is the lower limit of the integral, which must be varied to determine the true radiative open-circuit voltage $V_{\text{oc}}^{\text{rad}}$, as described in the work of Zarrabi et al..^[20] It must be stressed that $V_{\text{oc}}^{\text{rad}}$ is *not* a spectral quantity; varying the lower limit of the integral just makes it appear that way. The true $V_{\text{oc}}^{\text{rad}}$ in the thermodynamic limit can be extracted from plots like the right-hand graph in the left pane of **Figure S8** by identifying the point where a plateau is reached. Using this $V_{\text{oc}}^{\text{rad}}$, the non-radiative open-circuit voltage loss under one-Sun conditions can be extracted using $\Delta V_{\text{oc}}^{\text{nr}} = V_{\text{oc}}^{\text{rad}} - V_{\text{oc}}^{\odot}$. Assuming this $\Delta V_{\text{oc}}^{\text{nr}}$ is the minimum open-circuit voltage experienced by the device under any set of illumination conditions, then the figures-of-merit can be predicted in indoor conditions using the approach outlined in **Section S2**, as illustrated in the left-hand pane of **Figure S8**.

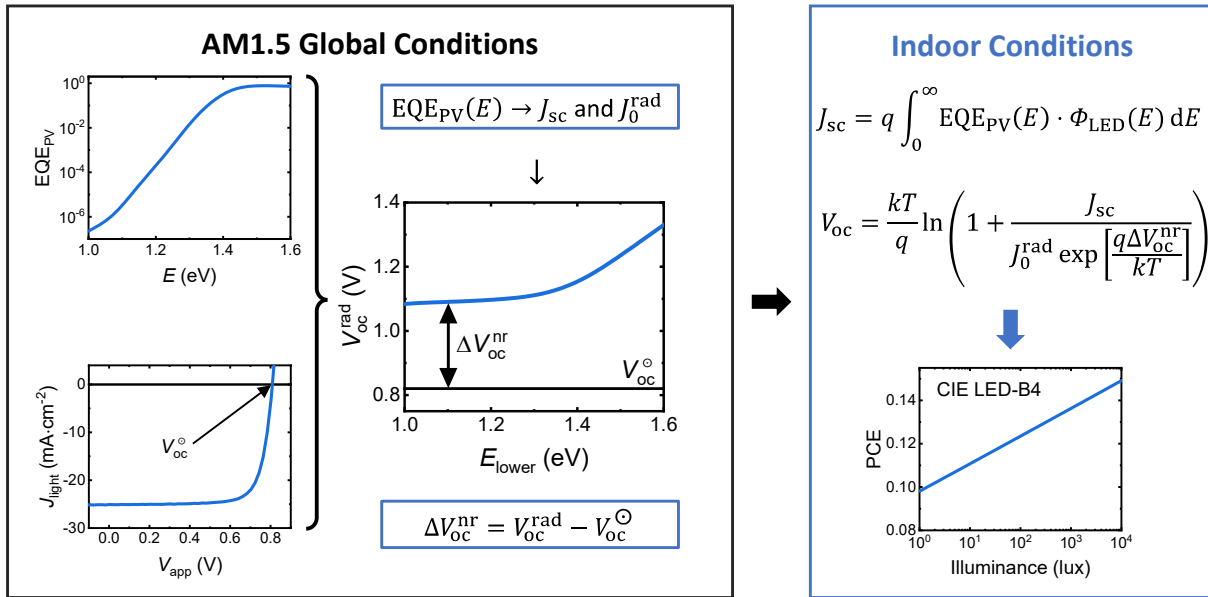


Figure S8: A block diagram illustrating how one-Sun (AM1.5 global) measurements can be used to predict device performance under indoor conditions. The left-hand pane shows how a photovoltaic external quantum efficiency spectrum and a current-density curve can be used, in combination, to extract the true $V_{\text{oc}}^{\text{rad}}$ which, in turn, can be used to evaluate the non-radiative open-circuit voltage loss, $\Delta V_{\text{oc}}^{\text{nr}}$. This loss is then carried across to the right-hand pane, illustrating the calculation of figures-of-merit under arbitrary indoor conditions.

S9. Extracting Parameters from Photovoltaic External Quantum Efficiency Spectra

For each of the OPV systems considered in this work, the optical gap and energetic disorder were determined using a methodology outlined in prior work by the authors.^[14] In that work, photovoltaic external quantum efficiency spectrum were fit with

$$\text{EQE}_{\text{PV}}(E) = \text{EQE}_0[1 - \exp(-\alpha(E)d)], \quad (\text{S31})$$

where EQE_0 is a pre-factor, d is the active layer thickness, and α is the exciton absorption coefficient. In this work, however, we make use of the weak αd limit (valid well below the gap) to write $\text{EQE}_{\text{PV}}(E)$ as seen in Equation (S13).^[21] In this limit, the apparent Urbach energy ($E_{\text{U}}^{\text{app}}$), defined by^[13, 22]

$$E_{\text{U}}^{\text{app}}(E) = \left[\frac{\partial \ln(\text{EQE}_{\text{PV}}(\epsilon))}{\partial \epsilon} \right]^{-1} \bigg|_{\epsilon=E}, \quad (\text{S32})$$

may be approximated with

$$E_{\text{U}}^{\text{app}}(E) \approx kT \left[1 + \frac{1 + \text{erf}\left(\frac{E - E_{\text{opt}}}{\sigma_s \sqrt{2}}\right)}{\exp\left(\frac{E - E_{\text{opt}} + \frac{\sigma_s^2}{2kT}}{kT}\right) \text{erfc}\left(\frac{E - E_{\text{opt}} + \frac{\sigma_s^2}{kT}}{\sigma_s \sqrt{2}}\right)} \right]. \quad (\text{S33})$$

Note that $E_{\text{opt}} \gg \sigma_s$ has been assumed. The spectral behavior of Equation (S33) is plotted normalized to the thermal energy kT for varied E_{opt} in **Figure S9a**, and for varied σ_s in **Figure S9b**. From these graphs, it can be seen that well below the gap, $E_{\text{U}}^{\text{app}} \rightarrow kT$, regardless of the σ_s value. Furthermore, as $E \rightarrow E_{\text{opt}}$, the apparent Urbach energy tends to infinity; a shift in E_{opt} corresponds with an equivalent shift in the $E_{\text{U}}^{\text{app}}$ spectrum. Whereas a change in σ_s on the other hand corresponds with a broadened transition between the $E_{\text{U}}^{\text{app}} = kT$ and the $E_{\text{U}}^{\text{app}} \rightarrow \infty$ regimes.

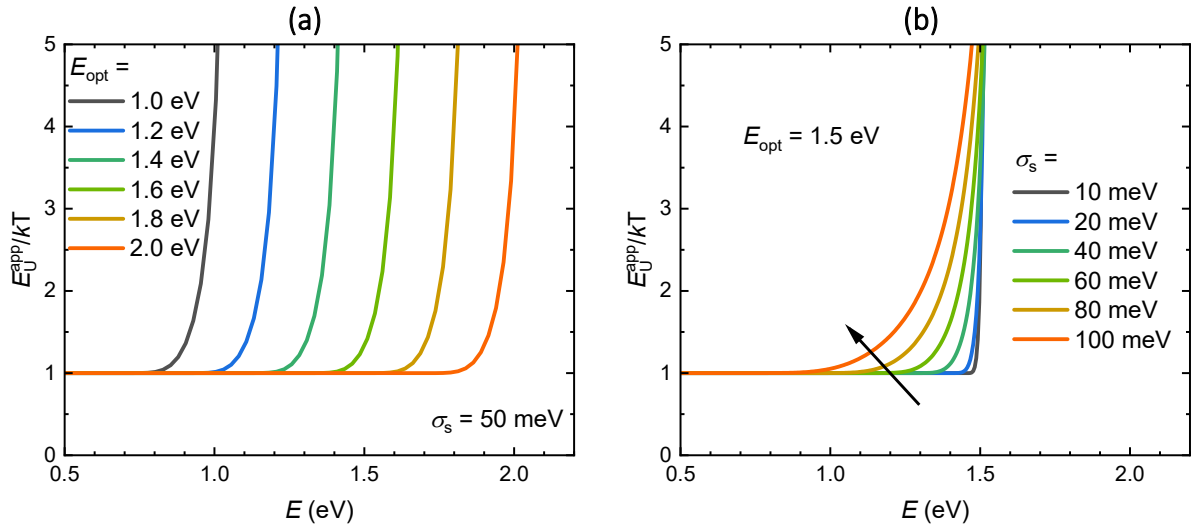


Figure S9: The apparent Urbach energy approximation given by Equation (S30), plotted normalized to the thermal energy kT as a function of the photon energy E , for varied E_{opt} in (a) and varied σ_s in (b).

Using Equation (S33), the optical gap and energetic disorder of several technologically-relevant donor:acceptor OPV blends were estimated using their apparent Urbach spectra, which were determined from the corresponding reported EQE_{PV} spectra using Equation (S32). The EQE_{PV} spectra themselves were also fit with the methodology outlined in our previous work.^[14] The extracted values are inserted into the respective graphs throughout the remainder of this section, with the values extracted using Equation (S33) likely to be more accurate due to one of the free parameters, EQE_{max}, being removed from the fitting. The spectra are plotted in **Figure S10** to **Figure S18**; the extracted values are summarized in **Table S4**.

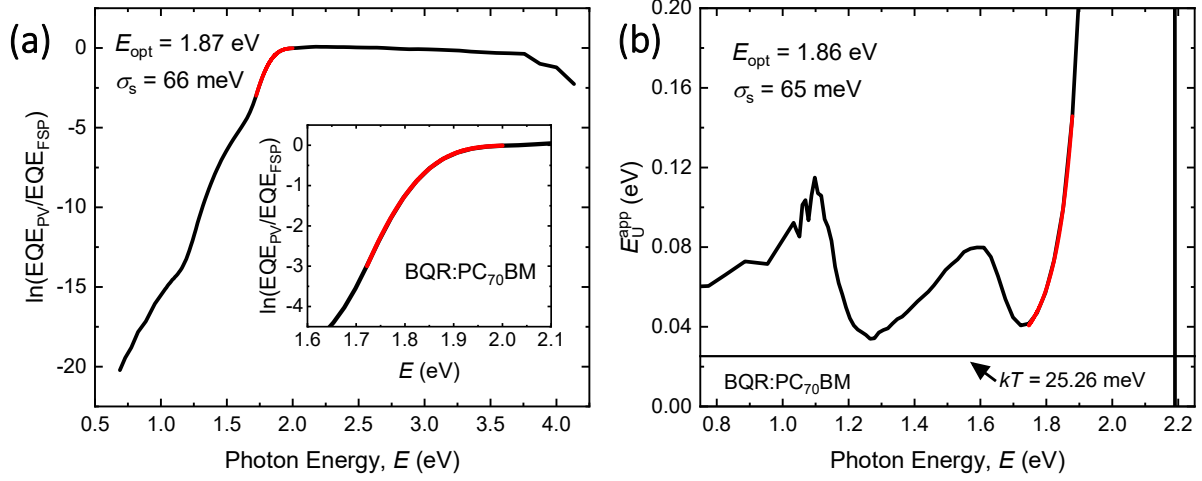


Figure S10: Experimentally-determined and simulated parameters for BQR:PC₇₀BM (a) The experimentally-determined photovoltaic external quantum efficiency spectrum, normalized to its value at the first saturation peak (EQE_{FSP}) and (b) its corresponding apparent Urbach energy spectrum. Both spectra are fit with their respective models – the extracted values for the narrower optical gap component (PC₇₀BM) are included.

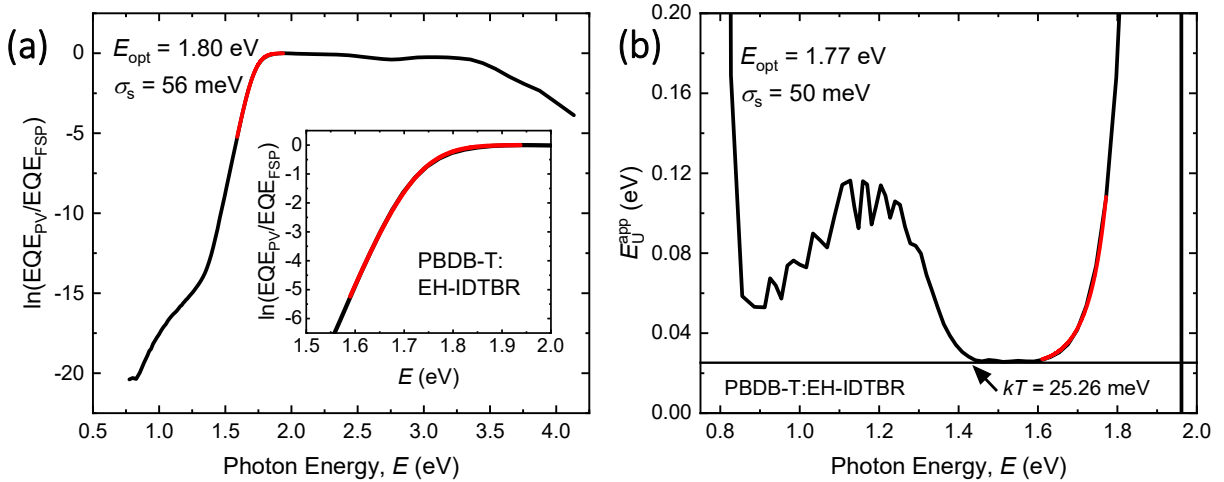


Figure S11: (a) The photovoltaic external quantum efficiency spectrum for PBDB-T:EH-IDTBR, normalized to its value at the first saturation peak (EQE_{FSP}) and (b) its corresponding apparent Urbach energy spectrum. As illustrated by the red curves, both spectra are fit with their respective models – EQE_{PV}

with the methodology outlined in our previous work^[14] and E_U^{app} with Equation (S33) – and the extracted values for the narrower optical gap component (EH-IDTBR) are included.

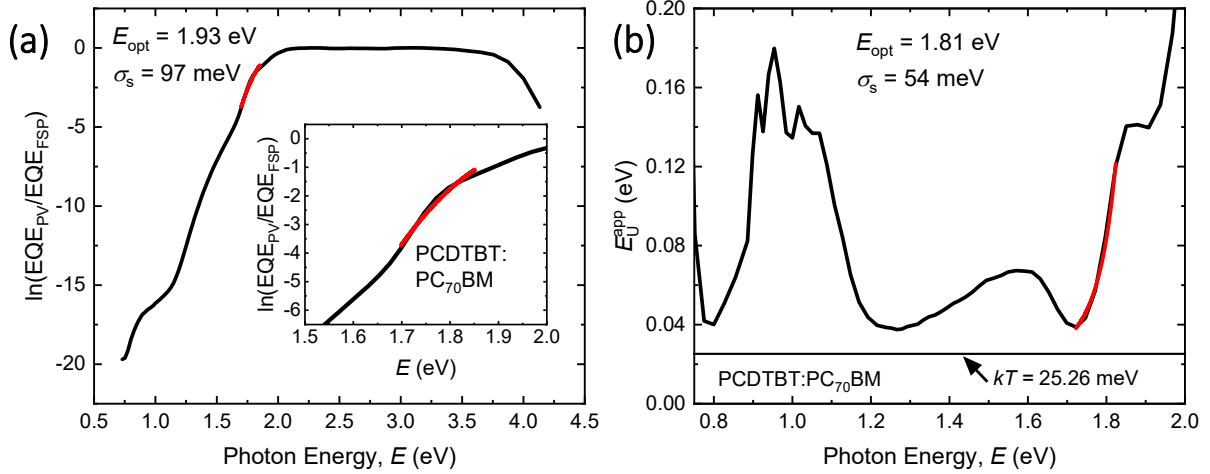


Figure S12: (a) The photovoltaic external quantum efficiency spectrum for PCDTBT:PC₇₀BM, normalized to its value at the first saturation peak (EQE_{FSP}) and (b) its corresponding apparent Urbach energy spectrum. As illustrated by the red curves, both spectra are fit with their respective models – EQE_{PV} with the methodology outlined in our previous work^[14] and E_U^{app} with Equation (S33) – and the extracted values for the narrower optical gap component (PCDTBT) are included.

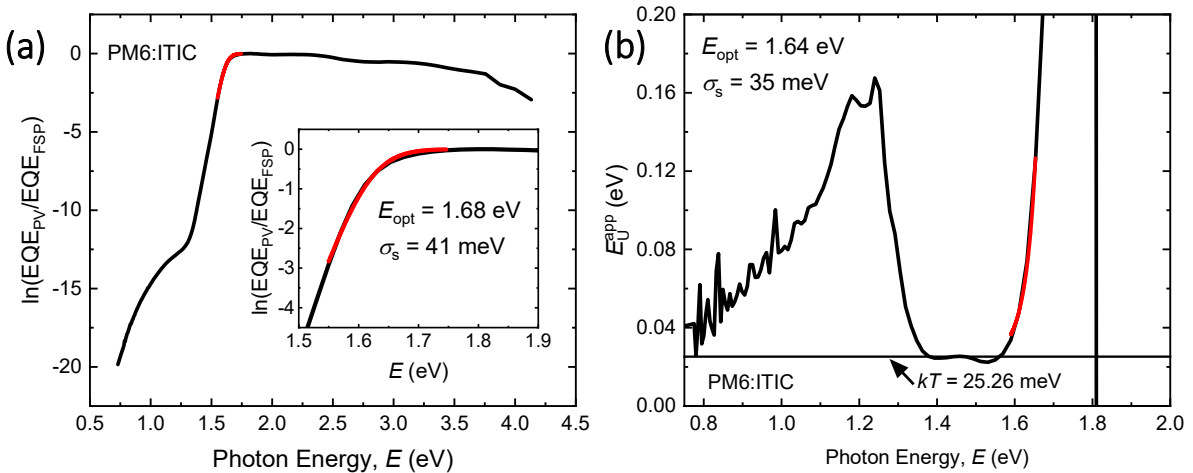


Figure S13: (a) The photovoltaic external quantum efficiency spectrum for PM6:ITIC, normalized to its value at the first saturation peak (EQE_{FSP}) and (b) its corresponding apparent Urbach energy spectrum. As illustrated by the red curves, both spectra are fit with their respective models – EQE_{PV} with the methodology outlined in our previous work^[14] and $E_{\text{U}}^{\text{app}}$ with Equation (S33) – and the extracted values for the narrower optical gap component (ITIC) are included.

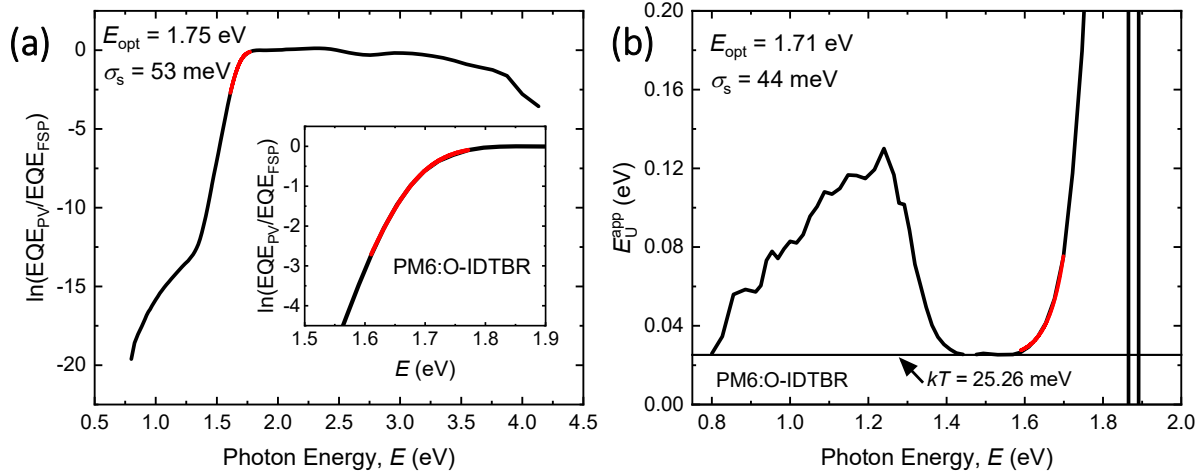


Figure S14: (a) The photovoltaic external quantum efficiency spectrum for PM6:O-IDTBR, normalized to its value at the first saturation peak (EQE_{FSP}) and (b) its corresponding apparent Urbach energy spectrum. As illustrated by the red curves, both spectra are fit with their respective models – EQE_{PV} with the methodology outlined in our previous work^[14] and $E_{\text{U}}^{\text{app}}$ with Equation (S33) – and the extracted values for the narrower optical gap component (O-IDTBR) are included.

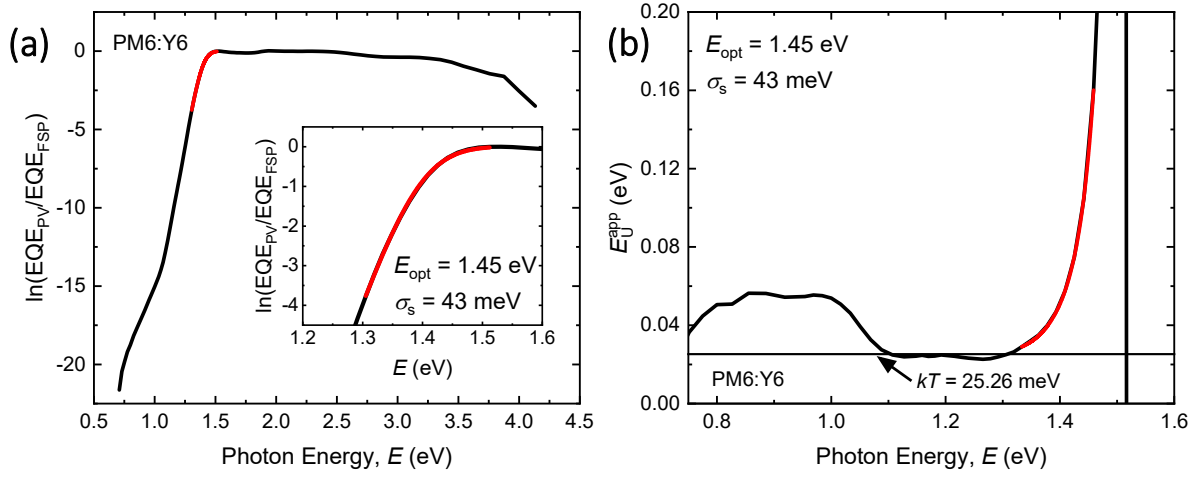


Figure S15: (a) The photovoltaic external quantum efficiency spectrum for PM6:Y6, normalized to its value at the first saturation peak (EQE_{FSP}) and (b) its corresponding apparent Urbach energy spectrum. As illustrated by the red curves, both spectra are fit with their respective models – EQE_{PV} with the methodology outlined in our previous work^[14] and E_U^{app} with Equation (S33) – and the extracted values for the narrower optical gap component (Y6) are included.

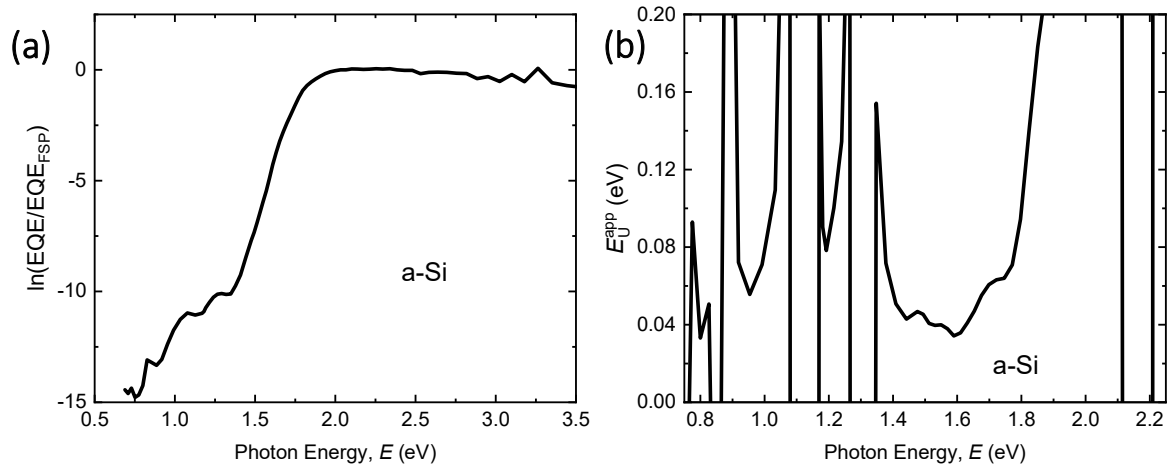


Figure S16: (a) The photovoltaic external quantum efficiency spectrum normalized to its first saturation peak value (EQE_{FSP}) and (b) the resultant apparent Urbach energy spectrum for amorphous silicon (a-Si). While these spectra were used to estimate the indoor performance, the optical gap was referenced from the literature.^[23]

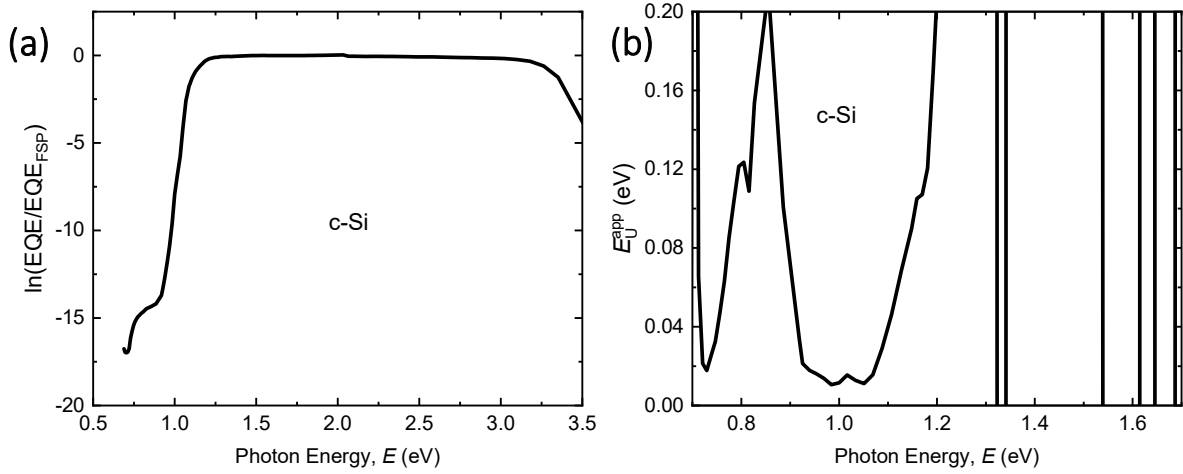


Figure S17: (a) The photovoltaic external quantum efficiency spectrum normalized to its first saturation peak value (EQE_{FSP}) and (b) the resultant apparent Urbach energy spectrum for crystalline silicon (c-Si). While these spectra were used to estimate the indoor performance, the optical gap was referenced from the literature. ^[23]

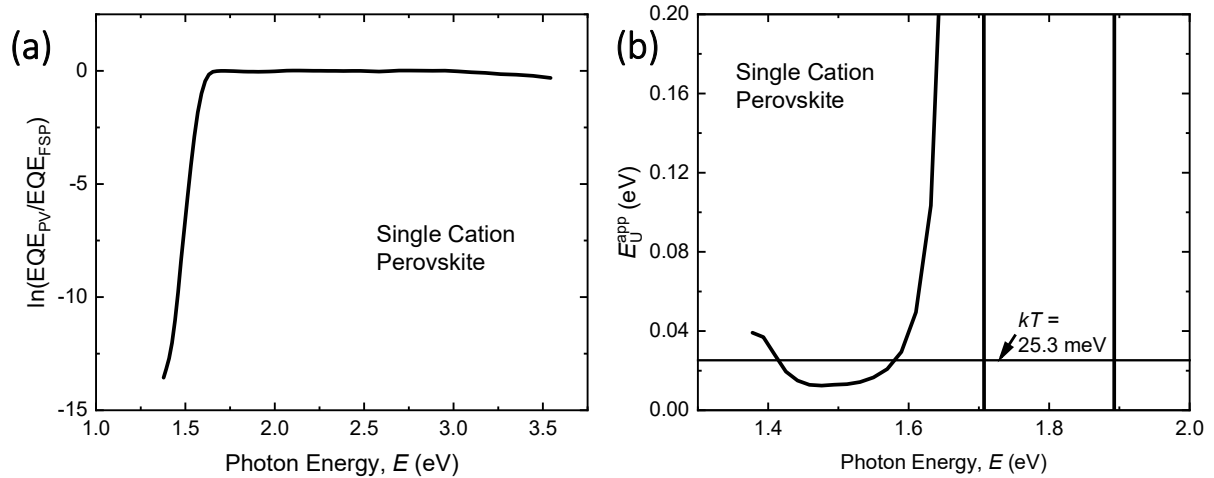


Figure S18: (a) The photovoltaic external quantum efficiency spectrum normalized to its first saturation peak value (EQE_{FSP}) and (b) the resultant apparent Urbach energy spectrum for a single cation perovskite device. ^[17] This spectrum was used to estimate the indoor performance of the device; its optical gap is around 1.61 eV, ^[24] and its Urbach was previously found to be $E_U = 13.0 \text{ meV}$ (around half the thermal energy, kT). ^[17, 24]

Table S4: Optical gap (E_{opt}) and excitonic static disorder (σ_s) values extracted from apparent Urbach energy spectra of **Figure S10-S18**. For the OPV systems, the values correspond to the narrower optical gap components of each respective blend, which have been underlined in the first column for clarity.

System	E_{opt} (eV)	σ_s (meV) ^a
Crystalline Silicon	1.12 ^[5]	-
Amorphous Silicon	1.60 ^[23]	-
Single Cation Perovskite	1.61 ^[24]	-
PM6: <u>Y6</u>	1.44	43
PBDB-T: <u>EH-IDTBR</u>	1.77	50
PM6: <u>BTP-eC9</u>	1.42	43
PM6: <u>ITIC</u>	1.64	35
PM6: <u>O-IDTBR</u>	1.71	44
BQR: <u>PC₇₀BM</u>	1.86	65
<u>PCDTBT</u> :PC ₇₀ BM	1.81	54

a – Excitonic static disorder values quoted estimated only for organic systems

S10. Estimating Indoor Performance for a Variety of Systems

For each of the donor:acceptor blends considered in this work, the short-circuit current density, radiative dark saturation current density, and radiative open-circuit voltage were determined using techniques previously published by the authors.^[20] As summarized in **Section S7**, the non-radiative losses can then be extracted using the open-circuit voltage under one-Sun conditions (denoted as V_{oc}^{\odot}) and the radiative open-circuit voltage. The values for the photovoltaic materials considered in this work are summarized in **Table S5**.

Table S5. Non-radiative open-circuit voltage losses ($\Delta V_{\text{oc}}^{\text{nr}}$) for a variety of photovoltaics, including donor:acceptor OPV blends. The values were determined by subtracting experimentally-determined open-circuit voltage values under one Sun-conditions V_{oc}^{\odot} from the radiative open-circuit voltage determined using each blend's photovoltaic external quantum efficiency spectrum.

System	Experimental V_{oc}^{\odot} (V)	E_{lower} (eV)	J_{sc}^{\odot} (mA · cm ⁻²)	$V_{\text{oc}}^{\text{rad}}$ (V)	$\Delta V_{\text{oc}}^{\text{nr}}$ (V)
Crystalline Silicon	0.66 ^[20]	0.81	38.1	0.863	0.203
Amorphous Silicon	0.90 ^[25]	1.41	1.82	1.347	0.447
Single Cation Perovskite	1.10 ^[17]	1.38	21.3	1.311	0.211
PM6:Y6	0.82 ^[20]	1.20	22.9	1.097	0.277
PBDB-T:EH-IDTBR	0.98 ^[26]	1.44	10.5	1.387	0.407
PM6:BTP-eC9	0.83 ^[26]	1.18	24.8	1.084	0.254
PM6:ITIC	0.98 ^[20]	1.39	10.3	1.300	0.320
PM6:O-IDTBR	1.07 ^[26]	1.44	4.7	1.351	0.281
BQR:PC ₇₀ BM	0.91 ^[26]	1.70	9.5	1.488	0.578
PCDTBT:PC ₇₀ BM	0.82 ^[20]	1.24	6.7	1.270	0.450

Table S6. Power conversion efficiencies for each of photovoltaic materials considered in this work (before scaling J_{sc} with literature values) under one-Sun conditions, and under the 2700K LED, the 4000K LED, and the CIE LED-B4 at 500 lux illuminations. The non-radiative open-circuit voltage loss for each blend has been assigned using **Table S5**.

System	E_{lower} (eV)	PCE			
		One-Sun (AM1.5G @ 100mW/cm²)	2700K LED @ 500 lux	4000K LED @ 500 lux	CIE LED-B4 @ 500 lux
Crystalline Silicon	0.81	0.211	0.179	0.164	0.165
Amorphous Silicon	1.41	0.0143	0.0277	0.0267	0.0265
Single Cation Perovskite	1.38	0.210	0.342	0.323	0.322
PM6:Y6	1.20	0.162	0.200	0.181	0.162
PBDB-T:EH-IDTBR	1.44	0.091	0.178	0.161	0.160
PM6:BTP-eC9	1.18	0.179	0.211	0.191	0.179
PM6:ITIC	1.39	0.089	0.153	0.136	0.136
PM6:O-IDTBR	1.44	0.045	0.084	0.077	0.077
BQR:PC ₇₀ BM	1.20	0.076	0.146	0.143	0.141
PCDTBT:PC ₇₀ BM	1.24	0.048	0.084	0.089	0.087

S11. Scaling Estimated Performance to Literature Values

For each photovoltaic material, following the calculation of its J_{sc} under one-Sun conditions (J_{sc}^{\odot}), a comparable, experimentally-determined value was found in the literature. If the short-circuit current density is multiplied by some factor A , which corresponds to the scaling of EQE_{PV} by A , then J_0 will also be receive an equivalent scaling. As V_{oc} and FF are then independent of A , a scaling of J_{sc} can be will equally scale the PCE. The scale factors for each of the photovoltaic materials considered in this work are compiled in

Table S7. The corresponding scaled power conversion efficiencies are summarized in **Table S8**.

Table S7: Scale factors for scaling short-circuit current densities to match best values of the literature.

The references are provided in the fourth column of the table whereas the scale factors are in the fifth column.

System	Calculated J_{sc}^{\odot} (mA · cm ⁻²)	Literature J_{sc}^{\odot} (mA · cm ⁻²)	Reference	Scale Factor
Crystalline Silicon	38.1	42.9	[25]	1.13
Amorphous Silicon	1.82	16.7	[25]	9.18
Single Cation Perovskite	21.3	21.3	[17]	1
PM6:Y6	22.9	26.9	[27]	1.17
PBDB-T:EH-IDTBR	10.5	15.6	[28]	1.49
PM6:BTP-eC9	24.8	25.1	[29]	1.01
PM6:ITIC	10.3	16.0	[30]	1.55
PM6:O-IDTBR	4.7	15.2	[31]	3.23
BQR:PC ₇₀ BM	9.5	15.3	[32]	1.61
PCDTBT:PC ₇₀ BM	6.7	12.1	[33]	1.81

Table S8: The scaled power conversion efficiencies under one-Sun, 2700K LED, 4000K LED, and CIE

LED-B4 illumination. The non-scaled are summarized in **Table S6**, whereas the scale factors are summarized in **Table S7**.

		Scaled PCE			
System	Scale Factor	One-Sun (AM1.5G @ 100mW/cm ²)	2700K LED @ 500 lux	4000K LED @ 500 lux	CIE LED-B4 @ 500 lux
Crystalline Silicon	1.13	0.238	0.202	0.185	0.186
Amorphous Silicon	9.18	0.131	0.254	0.245	0.243
Single Cation Perovskite	1	0.210	0.342	0.323	0.322
PM6:Y6	1.17	0.190	0.234	0.212	0.190
PBDB-T:EH-IDTBR	1.49	0.136	0.265	0.240	0.238
PM6:BTP-eC9	1.01	0.181	0.213	0.193	0.181
PM6:ITIC	1.55	0.138	0.237	0.210	0.211
PM6:O-IDTBR	3.23	0.145	0.271	0.249	0.249
BQR:PC ₇₀ BM	1.61	0.122	0.235	0.230	0.227
PCDTBT:PC ₇₀ BM	1.81	0.087	0.152	0.161	0.157

Appendix – Dark Saturation Current Density in Organic Photovoltaics

In the weak absorption limit, we take the spectral lineshape of the sub-gap photovoltaic external quantum efficiency to be given by Equation (S13). The corresponding dark saturation current density in the radiative limit will be given by

$$J_0^{\text{rad}} \approx \frac{EQE_{\text{max}}\pi q}{h^3 c^2} \int_0^{\infty} E^2 \exp\left(-\frac{E}{kT}\right) \left[\exp\left(\frac{E - E_{\text{opt}} + \frac{\sigma_s^2}{2kT}}{kT}\right) \text{erfc}\left(\frac{E - E_{\text{opt}} + \frac{\sigma_s^2}{kT}}{\sigma_s \sqrt{2}}\right) \right. \\ \left. + \text{erf}\left(\frac{E_{\text{opt}}}{\sigma_s \sqrt{2}}\right) + \text{erf}\left(\frac{E - E_{\text{opt}}}{\sigma_s \sqrt{2}}\right) \right] dE. \quad (\text{A1})$$

This integral can be evaluated in three parts, the simplest of which is evaluated using the gamma function:

$$\int_0^{\infty} E^2 \exp\left(-\frac{E}{kT}\right) dE = 2(kT)^3. \quad (\text{A2})$$

The next integral may be evaluated by-parts, where the derivative of the error function needs to be taken.

With $x = \frac{E}{\sigma_s \sqrt{2}}$ and $\Delta = -E_{\text{opt}} + \frac{\sigma_s^2}{kT}$, this gives

$$\int_0^{\infty} E^2 \text{erfc}\left(\frac{E - E_{\text{opt}} + \frac{\sigma_s^2}{kT}}{\sigma_s \sqrt{2}}\right) dE = \frac{2(\sigma_s \sqrt{2})^3}{3\sqrt{\pi}} \int_0^{\infty} x^3 \exp\left(-\left[x + \frac{\Delta}{\sigma_s \sqrt{2}}\right]^2\right) dx \\ = \frac{(\sigma_s \sqrt{2})^3}{3} \left(\frac{1}{\sqrt{\pi}} \left[1 + \frac{\Delta^2}{2\sigma_s^2} \right] \exp\left(-\frac{\Delta^2}{2\sigma_s^2}\right) - \frac{\Delta}{\sigma_s \sqrt{2}} \left[\frac{3}{2} + \frac{\Delta^2}{2\sigma_s^2} \right] \text{erfc}\left(\frac{\Delta}{\sigma_s \sqrt{2}}\right) \right). \quad (\text{A3})$$

To obtain the final line, the following integrals were used:

$$\int e^{-x^2} dx = \frac{\sqrt{\pi}}{2} \text{erf}(x) + C, \quad (\text{A4a})$$

$$\int x e^{-x^2} dx = -\frac{e^{-x^2}}{2} + C, \quad (\text{A4b})$$

$$\int x^n e^{-x^2} dx = -\frac{x^{n-1} e^{-x^2}}{2} + \frac{(n-1)}{2} \int x^{n-2} e^{-x^2} dx, \quad \text{for } n \geq 2 \quad (\text{A4c})$$

The final of the three integrals is the most involved. With some variable substitutions $x = \frac{E}{kT}$, $\delta = -\frac{E_{\text{opt}}}{\sigma_s \sqrt{2}}$,

and $r = \frac{kT}{\sigma_s \sqrt{2}}$, integration by parts gives

$$\begin{aligned} & \int_0^\infty E^2 \operatorname{erf}\left(\frac{E - E_{\text{opt}}}{\sigma_s \sqrt{2}}\right) \exp\left(-\frac{E}{kT}\right) dE \\ &= (kT)^3 \left(2 \operatorname{erf}(\delta) \right. \\ & \quad \left. + \frac{2r}{\sqrt{\pi}} \exp\left(\frac{\Delta^2 - E_{\text{opt}}^2}{2\sigma_s^2}\right) \int_0^\infty [x^2 + 2x + 2] \exp\left(-\left[rx + \frac{\Delta}{\sigma_s \sqrt{2}}\right]^2\right) dx \right). \end{aligned} \quad (\text{A5})$$

The integrals can be evaluated as above. After combining with the result of the first integral, making use of the fact that the error function is an odd function, and simplifying, one finds

$$\begin{aligned} & \operatorname{erf}\left(\frac{E_{\text{opt}}}{\sigma_s \sqrt{2}}\right) \int_0^\infty E^2 \exp\left(-\frac{E}{kT}\right) dE + \int_0^\infty E^2 \operatorname{erf}\left(\frac{E - E_{\text{opt}}}{\sigma_s \sqrt{2}}\right) \exp\left(-\frac{E}{kT}\right) dE \\ &= \exp\left(\frac{\Delta^2 - E_{\text{opt}}^2}{2\sigma_s^2}\right) \left(\sigma_s \sqrt{\frac{2}{\pi}} [-\Delta kT + 2(kT)^2] \exp\left(\frac{\Delta^2}{2\sigma_s^2}\right) \right. \\ & \quad \left. + [kT(\Delta^2 + \sigma_s^2) - 2\Delta(kT)^2 + 2(kT)^3] \operatorname{erfc}\left(\frac{\Delta}{\sigma_s \sqrt{2}}\right) \right). \end{aligned} \quad (\text{A6})$$

Finally, combining all the pieces gives the full expression for the dark saturation current density,

$$\begin{aligned} J_0^{\text{rad}} \approx & \frac{\text{EQE}_{\text{max}} \pi q}{h^3 c^2} \exp\left(\frac{-E_{\text{opt}} + \frac{\sigma_s^2}{2kT}}{kT}\right) \left[\sigma_s \sqrt{\frac{2}{\pi}} \left(\frac{\Delta^2}{3} - \Delta kT + 2k^2 T^2 + \frac{2\sigma_s^2}{3} \right) \cdot \exp\left(-\frac{\Delta^2}{2\sigma_s^2}\right) \right. \\ & \quad \left. + \left((\Delta^2 + \sigma_s^2)kT - \Delta[2k^2 T^2 + \sigma_s^2] + 2k^3 T^3 - \frac{\Delta^3}{3} \right) \operatorname{erfc}\left(\frac{\Delta}{\sigma_s \sqrt{2}}\right) \right]. \end{aligned} \quad (\text{A7})$$

References

1. Sze, S.M., Y. Li, and K.K. Ng, *Physics of Semiconductor Devices*. Fourth Edition ed. **2021**: John Wiley & Sons, Inc.
2. Burwell, G., O.J. Sandberg, W. Li, P. Meredith, M. Carnie, and A. Armin, *Scaling Considerations for Organic Photovoltaics for Indoor Applications*. Solar RRL, **2022**. 6(7): p. 2200315.
3. Stockman, A., H. Jägle, M. Pirzer, and L.T. Sharpe, *The Dependence of Luminous Efficiency on Chromatic Adaptation*. Journal of Vision, **2008**. 8(16): p. 1-1.
4. Köhler, A. and H. Bässler, *Electronic Processes in Organic Semiconductors: An Introduction*. **2015**: John Wiley & Sons.
5. Nelson, J.A., *The Physics of Solar Cells*. **2003**: World Scientific Publishing Company.
6. Vandewal, K., K. Tvingstedt, A. Gadisa, O. Inganäs, and J.V. Manca, *Relating the Open-Circuit Voltage to Interface Molecular Properties of Donor:Acceptor Bulk Heterojunction Solar Cells*. Physical Review B, **2010**. 81(12): p. 125204.
7. Valluri, S.R., D.J. Jeffrey, and R.M. Corless, *Some Applications of the Lambert W Function to Physics*. Canadian Journal of Physics, **2000**. 78(9): p. 823-831.
8. Corless, R.M., G.H. Gonnet, D.E. Hare, D.J. Jeffrey, and D.E. Knuth, *On the Lambert W function*. Advances in Computational mathematics, **1996**. 5(1): p. 329-359.
9. Fathabadi, H., *Lambert W Function-Based Technique for Tracking the Maximum Power Point of PV Modules Connected in Various Configurations*. Renewable Energy, **2015**. 74: p. 214-226.
10. Roibás-Millán, E., J.L. Cubero-Estalrich, A. Gonzalez-Estrada, R. Jado-Puente, M. Sanabria-Pinzón, D. Alfonso-Corcuera, J.M. Álvarez, J. Cubas, and S. Pindado. *Lambert W-function Simplified Expressions for Photovoltaic Current-Voltage Modelling*. in *2020 IEEE International Conference on Environment and Electrical Engineering and 2020 IEEE Industrial and Commercial Power Systems Europe (EEEIC / I&CPS Europe)*. **2020**.
11. Ryaben'kii, V.S. and S.V. Tsynkov, *A Theoretical Introduction to Numerical Analysis*. **2006**: Chapman and Hall/CRC.
12. Würfel, P. and U. Würfel, *Physics of Solar Cells: From Basic Principles to Advanced Concepts*. **2016**: John Wiley & Sons.
13. Kaiser, C., O.J. Sandberg, N. Zarrabi, W. Li, P. Meredith, and A. Armin, *A Universal Urbach Rule for Disordered Organic Semiconductors*. Nature Communications, **2021**. 12(1): p. 3988.
14. Kay, A.M., O.J. Sandberg, N. Zarrabi, W. Li, S. Zeiske, C. Kaiser, P. Meredith, and A. Armin, *Quantifying the Excitonic Static Disorder in Organic Semiconductors*. Advanced Functional Materials, **2022**. 32(32): p. 2113181.
15. Riley, K.F. and M.P. Hobson, *Essential Mathematical Methods for the Physical Sciences*. **2011**: Cambridge University Press.
16. Urbach, F., *The Long-Wavelength Edge of Photographic Sensitivity and of the Electronic Absorption of Solids*. Physical Review, **1953**. 92(5): p. 1324-1324.
17. Zeiske, S., O.J. Sandberg, N. Zarrabi, C.M. Wolff, M. Raoufi, F. Peña-Camargo, E. Gutierrez-Partida, P. Meredith, M. Stolterfoht, and A. Armin, *Static Disorder in Lead Halide Perovskites*. The Journal of Physical Chemistry Letters, **2022**. 13(31): p. 7280-7285.
18. Planck, M., *The Theory of Heat Radiation*. **1914**: Blakiston.
19. Rau, U., *Reciprocity Relation Between Photovoltaic Quantum Efficiency and Electroluminescent Emission of Solar Cells*. Physical Review B, **2007**. 76(8): p. 085303.
20. Zarrabi, N., O.J. Sandberg, S. Zeiske, W. Li, D.B. Riley, P. Meredith, and A. Armin, *Charge-Generating Mid-Gap Trap States Define the Thermodynamic Limit of Organic Photovoltaic Devices*. Nature Communications, **2020**. 11(1): p. 5567.

21. Armin, A., N. Zarrabi, O.J. Sandberg, C. Kaiser, S. Zeiske, W. Li, and P. Meredith, *Limitations of Charge Transfer State Parameterization Using Photovoltaic External Quantum Efficiency*. Advanced Energy Materials, **2020**. 10(41): p. 2001828.
22. Pankove, J.I., *Optical Processes in Semiconductors*. **1975**: Courier Corporation.
23. Mathews, I., S.N. Kantareddy, T. Buonassisi, and I.M. Peters, *Technology and Market Perspective for Indoor Photovoltaic Cells*. Joule, **2019**. 3(6): p. 1415-1426.
24. Dewi, H.A., J. Li, E. Erdenebileg, H. Wang, M. De Bastiani, S. De Wolf, N. Mathews, S. Mhaisalkar, and A. Bruno, *Efficient Bandgap Widening in Co-Evaporated MAPbI₃ Perovskite*. Sustainable Energy & Fuels, **2022**. 6(10): p. 2428-2438.
25. Green, M.A., E.D. Dunlop, G. Siefer, M. Yoshita, N. Kopidakis, K. Bothe, and X. Hao, *Solar Cell Efficiency Tables (Version 61)*. Progress in Photovoltaics: Research and Applications, **2003**.
26. Li, W., S. Zeiske, O.J. Sandberg, D.B. Riley, P. Meredith, and A. Armin, *Organic Solar Cells with Near-Unity Charge Generation Yield*. Energy & Environmental Science, **2021**. 14(12): p. 6484-6493.
27. Han, Y., H. Dong, W. Pan, B. Liu, X. Chen, R. Huang, Z. Li, F. Li, Q. Luo, J. Zhang, Z. Wei, and C.-Q. Ma, *An Efficiency of 16.46% and a T₈₀ Lifetime of Over 4000 h for the PM6:Y6 Inverted Organic Solar Cells Enabled by Surface Acid Treatment of the Zinc Oxide Electron Transporting Layer*. ACS Applied Materials & Interfaces, **2021**. 13(15): p. 17869-17881.
28. Bristow, H., K.J. Thorley, A.J.P. White, A. Wadsworth, M. Babics, Z. Hamid, W. Zhang, A.F. Paterson, J. Kosco, J. Panidi, T.D. Anthopoulos, and I. McCulloch, *Impact of Nonfullerene Acceptor Side Chain Variation on Transistor Mobility*. Advanced Electronic Materials, **2019**. 5(10): p. 1900344.
29. Yin, Z., S. Mei, P. Gu, H.-Q. Wang, and W. Song, *Efficient Organic Solar Cells with Superior Stability Based on PM6:BTP-eC9 Blend and AZO/Al Cathode*. iScience, **2021**. 24(9): p. 103027.
30. Wang, Y., Q. Fan, X. Guo, W. Li, B. Guo, W. Su, X. Ou, and M. Zhang, *High-performance nonfullerene polymer solar cells based on a fluorinated wide bandgap copolymer with a high open-circuit voltage of 1.04 V*. Journal of Materials Chemistry A, **2017**. 5(42): p. 22180-22185.
31. Hoefler, S., T. Rath, N. Pastukhova, E. Pavlica, D. Scheunemann, S. Wilken, B. Kunert, R. Resel, M. Hobisch, S. Xiao, G. Bratina, and G. Trimmel, *The Effect of Polymer Molecular Weight on the Performance of PTB7-Th:O-IDTBR Non-Fullerene Organic Solar Cells*. Journal of Materials Chemistry A, **2018**. 6.
32. Schwarz, K.N., P.B. Geraghty, V.D. Mitchell, S.-U.-Z. Khan, O.J. Sandberg, N. Zarrabi, B. Kudisch, J. Subbiah, T.A. Smith, B.P. Rand, A. Armin, G.D. Scholes, D.J. Jones, and K.P. Ghiggino, *Reduced Recombination and Capacitor-like Charge Buildup in an Organic Heterojunction*. Journal of the American Chemical Society, **2020**. 142(5): p. 2562-2571.
33. He, Z., C. Zhong, X. Huang, W.-Y. Wong, H. Wu, L. Chen, S. Su, and Y. Cao, *Simultaneous Enhancement of Open-Circuit Voltage, Short-Circuit Current Density, and Fill Factor in Polymer Solar Cells*. Advanced Materials, **2011**. 23(40): p. 4636-4643.